Convection Initiation Associated with a Boundary Layer Convergence Line over a Real-World Sharp Vegetation-Contrast Area

HONGJUN LIU,[a] ZHIYONG MENG,[a] YUNING ZHU,[a] AND YIPENG HUANG[b]

[a] *Department of Atmospheric and Oceanic Sciences, School of Physics, and China Meteorological Administration Tornado Key Laboratory, Peking University, Beijing, China*

[b] *Xiamen Key Laboratory of Straits Meteorology, Xiamen Meteorological Bureau, Xiamen, China*

(Manuscript received 26 March 2022, in final form 31 January 2023)

ABSTRACT: Convection initiation (CI) has remained a major challenge in weather forecasting worldwide. The Hetao area in North China, the location of Asia's largest irrigation area, contains highly heterogeneous vegetation where near-surface convergence lines (boundaries) parallel to the oasis–desert border often emerge over the desert and initiate convection. This study investigated the evolution of such a boundary and its influence on the CI process where a series of cells were successively initiated along the boundary on 4 June 2013. Our results indicated that uneven surface heating across the oasis–desert border produced mesoscale thermal circulation. The westerly oasis breeze in the thermal circulation converged with the southerly background wind and formed a boundary over the desert along the high-temperature contrast line. A middle-hemisphere westerly trough further enhanced uplift and facilitated CI. Our simulation revealed that the first 30-dBZ parcels in each cell originated from either the desert side at a low level or the oasis side at a middle level, rather than from the oasis at a low level, as indicated by previous idealized studies. Southerly low-level parcels veered above the boundary and experienced a longer lifting time over the desert, while western parcels originating from the oasis experienced a shorter lifting time and smaller vertical displacement, resulting in middle-level parcels instead of low-level parcels that reached their level of free convection. Even though CI occurred over a surface boundary without a near-surface stable layer, the inflow may have originated from middle levels rather than in contact with the surface.

SIGNIFICANCE STATEMENT: The purpose of this study is to understand the evolution of a real-world near-surface convergence line and the associated deep convection initiation (CI) along the border of Asia's largest irrigation area and the desert in northern China. Notably, previous works have mainly focused on shallow convection over uneven vegetation distributions based on idealized simulations, which may be quite different from real-world interactions between thermal circulation and background flow. Our results highlight different parcel sources in different convections initiated by the same convergence line, which is different from the idealized situation where parcels mainly originate from the low-level oasis side.

KEYWORDS: Convection lines; Mesoscale processes; Secondary circulation; Vegetation-atmosphere interactions; Topographic effects; Boundary layer

1. Introduction

Understanding convection initiation (CI) has been a major challenge in weather forecasting worldwide, as it requires air parcels to be lifted to saturation, reach the level of free convection (LFC), and finally develop into deep moist convection (Markowski and Richardson 2011). As an important lifting mechanism of CI, boundary layer convergence lines (hereafter referred to as boundaries) may occur via differential heating due to heterogeneous underlying surfaces (Gambill and Mecikalski 2011).

CI processes over heterogeneous underlying surfaces have been examined mainly in terms of sea–land circulation (Franchito et al. 1998; Miller et al. 2003; Gille 2005; Lin et al. 2008; Huang et al. 2010; Lu et al. 2010; Rani et al. 2010; Qian et al. 2012; Chen et al. 2016), lake–land circulation (Keen and Lyons 1978; Estoque 1981; Comer and Mckendry 1993; Baker et al. 2001; Koseki and Mooney 2019), and mountain–valley circulation (Goldreich et al. 1986; Lu and Turco 1994; Porson et al. 2007; Wang et al. 2015; Tian and Miao 2019; Yu et al. 2021). Sea breezes usually initiate convection through intersection with other triggering mechanisms, such as a horizontal convective roll (HCR; Fovell 2005; Bennett et al. 2006), thunderstorm outflows (Weckwerth and Parsons 2006) or Kelvin–Helmholtz instability billows (Crosman and Horel 2010). Under the influence of a highly unstable environment, convection can also be triggered along a single sea breeze (Lu et al. 2012). Lake and valley breezes exhibit structures similar to those of sea breezes, but their updrafts are generally weaker and not sufficient to initiate convection alone. Lake and valley breezes often trigger convection through intersection with other triggering mechanisms, such as different lake breezes (Zamuriano et al. 2019), sea breezes (Liang et al. 2017) or urban heat islands (Dou et al. 2015).

Nonuniform vegetation also represents one type of heterogeneous underlying surface. Nonuniform vegetation may cause a thermal gradient owing to nonuniformity in evapotranspiration (Lyons et al. 1996; Pielke 2001; Garcia-Carreras et al. 2010; Wright et al. 2017) and/or soil moisture (vegetation area is generally an irrigation area), which subsequently affects heat and

Corresponding author: Zhiyong Meng, zymeng@pku.edu.cn

DOI: 10.1175/MWR-D-22-0083.1

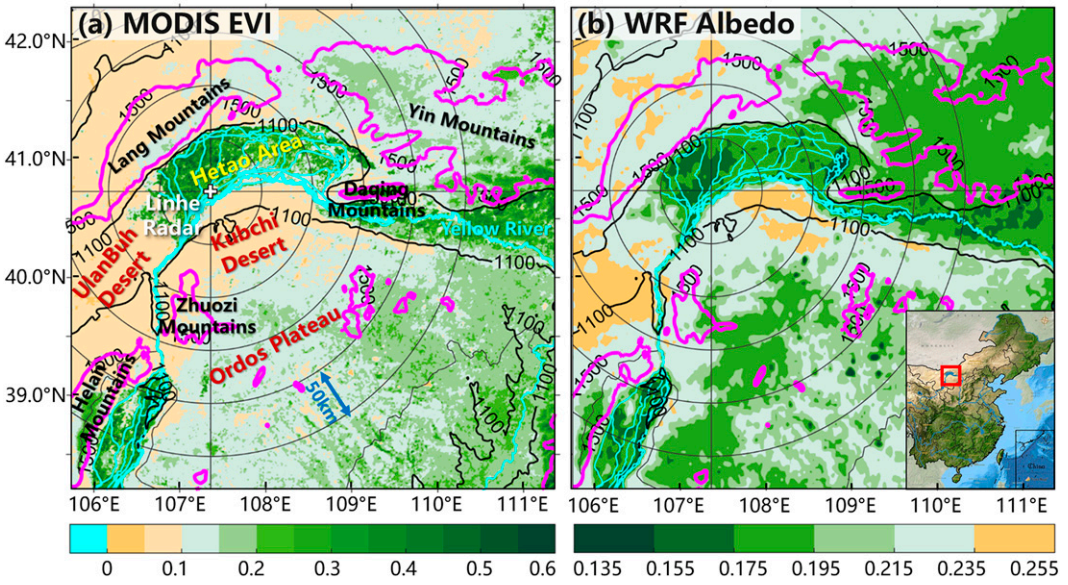

FIG. 1. (a) Distribution of the EVI (shading) and topography (black contours at 400-m intervals up to 1500 m, which is highlighted in magenta). (b) The simulated albedo (shading) and topography (contoured in black at 400-m intervals up to 1500 m, which is highlighted in magenta). The cyan lines denote the Yellow River, and the white cross in (a) denotes the LHRD radar site. The location of the displayed region is marked with a red rectangle in the lower-right corner of (b).

moisture fluxes in the planetary boundary layer (PBL) through turbulent transportation, producing thermal circulation. In areas with lower soil moisture, the latent heat flux is lower and the sensible heat flux is higher, which may result in ascending air, while in areas with higher soil moisture, descending air may occur (Ookouchi et al. 1984). Mesoscale thermal circulation attributed to the difference in soil moisture and the associated low-level convergence in dry areas and low-level divergence in wet areas have been observed over the Sahel (Taylor et al. 2007). Near the updraft branch over a dry area, when the PBL height is greater than the lifting condensation level (LCL), shallow cumulus convection may be initiated (Kang and Bryan 2011). Due to high turbulence over dry areas, water vapor is continuously transported upward, forming a mesoscale pool of cool and moist air just above the top of the PBL (Kang and Ryu 2016), which is a critical factor for the transition from shallow to deep convection (Zhang and Klein 2010). Statistical analysis has demonstrated that the probability of CI in areas with high soil moisture gradients was approximately twice that in areas with homogeneous soil moisture levels (Taylor et al. 2011). Under the influence of a gravity wave from a remote mature storm in the Sahel on 31 July 2006, a storm was initiated over the dry surface along a wet–dry soil boundary because of the associated low-level convergence, rather than soil moisture uniformity areas (Taylor et al. 2010). Real-world simulations of this storm suggested three aspects that need to be accurately represented in a model to predict these processes: the synoptic-scale circulation and thermodynamic environment, the land surface properties, especially soil moisture, to simulate the CI location properly, and the ability to capture gravity waves to simulate CI timing correctly (Birch et al. 2013).

Idealized simulations have demonstrated that the sources of moisture and unstable energy for CI over dry areas originate from wet areas. In dry areas, there is not enough native moisture to initiate convection (Seth and Giorgi 1996). At the edge of a given dry area, the surface breeze of thermal circulation transports moisture from wet to dry areas, and the ascending branch transports moisture upward, forming a humid environment conducive to CI (Courault et al. 2007; Seth and Giorgi 1996; Wang et al. 2011). Moreover, higher transpiration in wet areas increases the equivalent potential temperature θ_e and convective available potential energy (CAPE), and surface breezes advect high-θ_e air from wet to dry areas and vertically mix this air over the dry area (Garcia-Carreras et al. 2011; Pielke 2001). However, whether this process truly occurs in real-world deep moist convection initiation associated with nonuniform vegetation remains unclear.

The irrigation and bend areas of the Yellow River in Inner Mongolia, North China (hereafter referred to as the Hetao area), which is located in a semiarid climate zone (Qu et al. 2019), is an area containing highly heterogeneous vegetation, as revealed by the MODIS Enhanced Vegetation Index product MOD13A3 (EVI; Didan 2015; shading in Fig. 1a). There is an obvious vegetation difference between the wet area irrigated by the Yellow River and the two surrounding deserts, namely, the Kubchi Desert to the south and the UlanBuh Desert to the southwest. According to Zhang et al. (2020), the Hetao irrigation area is the largest irrigation district in Asia and one of the three largest irrigation areas in China. The Yellow River alluvial plain shows a good soil tillage performance, which makes it one of the most important areas for grain and oil commodities in China. In addition to the Kubchi

and Ulanbuh Deserts, the Hetao area is surrounded by Lang Mountains to the northwest, Daqing Mountains to the east, and Zhuozi Mountains to the southwest, thus producing a highly complex underlying surface.

In the Hetao area, satellite observation analyses have revealed that shallow cumulus convection over the irrigated area was significantly less notable than that over the surrounding deserts (Sato et al. 2007). This phenomenon might be attributed to the mesoscale thermal circulation resulting from the soil moisture difference between deserts and irrigated areas. Based on simulations of the conditions on 4 August 2005 using artificially enhanced vegetation sharpness, Kawase et al. (2008) obtained the thermal circulation across the irrigated area and UlanBuh Desert and shallow cumulus convection over the desert. Along the section crossing the border between the UlanBuh Desert and irrigated areas, clear thermal circulation was captured with the rising branch over the desert and the sinking branch over the irrigated area. In their sensitivity experiment, where the soil moisture gradient was removed and the irrigated area was replaced with desert, no thermal circulation occurred, which verified that the above mesoscale thermal circulation was formed due to the oasis–desert thermal contrast. However, these studies only examined shallow cumulus convection rather than the initiation mechanism of deep moist convection in realistic vegetation sharpness. In addition, without radar observations, detailed features that appeared during the development of the examined convection processes were not revealed.

By examining radar observations in the Hetao area, Huang et al. (2019) noted the frequent occurrence of fine lines parallel to the vegetation border over the desert side and CI processes along these boundaries. A statistical analysis of the boundaries in the Hetao area was performed based on radar data from 2012 to 2016, and notably, more boundaries occurred in the desert area than in the irrigated area. These results demonstrated that most identified boundaries were parallel to the dominant vegetation contrast line. The development and evolution of these boundaries were consistent with the diurnal variation in the oasis–desert temperature difference. These boundaries could represent radar signatures of the updraft of the associated thermal circulation or oasis–desert breeze. Their results indicated that 44% of these boundaries were associated with CI, and the high-frequency center of the relevant convective precipitation coincided with the fine lines identified via radar at the junction of the irrigated and Kubchi Desert areas rather than the UlanBuh Desert area, as previously examined by Kawase et al. (2008). After initiation near the observed boundaries in the Hetao area, some convection may be strengthened downstream, resulting in severe disasters. For example, the extremely heavy rainfall that occurred in Beijing, China, on 21 July 2012 and caused 79 fatalities (Yu and Meng 2016) could be traced back to the Hetao area (Yu 2012; Meng et al. 2013). However, the detailed CI process, especially the impact of boundaries on the CI process in the Hetao area, remains unclear. Understanding the CI mechanism over the complicated underlying surface in the Hetao area could improve the understanding of the mesoscale thermal circulation and related CI processes attributed to real-world nonuniform vegetation, which could also aid in forecasting and early warnings of severe convection events in the Hetao and downstream areas.

The CI process typically results from a multiscale system interaction. The characteristics of the synoptic environment determine the formation potential of the boundary and convection initiation. Huang et al. (2022) examined the possible impact of different synoptic environments on the surface-driven boundary and the associated CI processes in the Hetao area. The synoptic environment was classified into five patterns. The probabilities of different patterns forming boundaries and initiating convections were related to synoptic-scale wind and mesoscale thermal circulation resulting from the heterogeneous vegetation. Similar to sea breezes (e.g., Arritt 1993; Atkins and Wakimoto 1997; Laird et al. 2001), an opposing (offshore for a sea breeze, southerly for an oasis breeze) ambient flow would converge with the onshore sea breeze (oasis breeze) and lead to enhancement of the horizontal land–sea (oasis–desert) temperature gradient. In contrast, a supporting (onshore for a sea breeze, northerly for an oasis breeze) ambient flow tends to disturb the temperature gradient.

This study aimed to examine the CI mechanism in a deep moist convection case associated with the boundary formed at the junction of the irrigated and Kubchi Desert areas on 4 June 2013 through observational analysis and real-world simulations. This case occurred in an environment pattern that has the largest frequency according to Huang et al. (2022). We attempted to answer the following two scientific questions: How did the boundary form and evolve? How did the boundary affect the resulting CI processes?

Section 2 introduces the data and methods used in this study. A case overview is presented in section 3. Section 4 analyzes the specific mechanism of boundary formation, evolution, and convection initiation based on real-world numerical simulations. Our conclusions and a discussion are provided in section 5.

2. Data and methods

This work employed radar data, surface observations and fifth-generation reanalysis (ERA5) data retrieved from the European Centre for Medium-Range Weather Forecasts (ECMWF) to obtain an overview of the boundary and related CI processes. The Linhe CD-band Doppler radar (LHRD; white cross in Fig. 1a) at 82 m AGL completes one volume scan approximately every 6 min, with nine elevations ranging from 0.5° to 19.5°. Surface observations at automatic weather stations of the China Meteorological Administration are available at 1-h intervals. The vegetation types were described with the MODIS monthly EVI product MOD13A3 with a horizontal resolution of 1 km (Didan 2015; shading in Fig. 1a). Topography data were adopted from ETOPO1 data in a 1-arcmin grid (National Geophysical Data Center/NESDIS/NOAA/U.S. Department of Commerce 2011; black and magenta contours in Fig. 1a).

The method of using radar echoes to identify boundaries was the same as that proposed by Huang et al. (2019). The boundary was identified as a linear area with composite

reflectivity at the lowest two elevations (0.5° and 1.5°) from −5 to 10 dBZ, with a width smaller than 10 km (Koch and Ray 1997), a length larger than 10 km and a duration longer than 6 min (Wilson and Schreiber 1986). The composite reflectivities at all nine elevations were used to identify convection. The first occurrence of 30 dBZ in the composite radar reflectivity was regarded as the threshold of CI (Wilson and Schreiber 1986).

The top and bottom heights above the radar level of the observed boundary were simply inferred from the radar reflectivity at different elevations with the four-thirds Earth radius model (Doviak and Zrnić 1993). Notably, the reflectivity is just an integrated history of the convergence and distribution of clear-air scatters and may not accurately reflect the true updraft depth. Since no other data were available, we only used reflectivity to provide a rough inference for the depth of the boundary. The height of target h was derived from radar-measurable parameters, elevation φ and the slant path of the composite radar reflectivities of the lowest two elevations that were larger than 0 dBZ r as follows:

$$h = [r^2 + (k_e a)^2 + 2rk_e \sin\varphi]^{1/2} - k_e a,$$

where a is the radius of Earth and k_e is a variable related to the vertical gradient of the atmospheric refractive index. A standard atmosphere was assumed in this study, which indicates that k_e is 4/3. The value 0 dBZ, rather than −5 dBZ, was chosen to distinguish between the boundary and the surrounding extensive −5 dBZ clutters that appeared after the boundary formed. The width of the observed boundary was also determined by 0 dBZ.

A 24-h real-world simulation was performed beginning at 2000 LST (LST = UTC + 8 h) 3 June 2013, which was ~12 h prior to formation of the boundary and ~19 h before CI, until 2000 LST 4 June using the WRF-ARW Model version 3.7.1 (Skamarock et al. 2008). The model was configured with four two-way nested domains (Fig. 2), which exhibited 27-, 9-, 3-, and 1-km horizontal grid spacings and 40 vertical levels. Final operational global analysis (FNL; National Centers for Environmental Prediction/National Weather Service/NOAA/U.S. Department of Commerce 2000) data gridded at 1° × 1° and 6-h intervals were used to provide the initial and lateral boundary conditions for the simulation. In all four domains, the simulation adopted the Morrison two-moment microphysics scheme (Morrison et al. 2009), the Asymmetrical Convective Model version 2 (ACM2) planetary boundary layer scheme (Pleim 2007), the CAM spectral-band longwave and shortwave schemes (Collins et al. 2004), and the Pleim–Xiu surface layer scheme (Pleim 2006). The Grell–Freitas cumulus parameterization scheme (Grell and Freitas 2014) was applied in domains D01 and D02, while no cumulus parameterization scheme was used in domains D03 and D04. The land surface model (LSM) adopted in this study was the Pleim–Xiu LSM (Pleim and Xiu 1995; Xiu and Pleim 2001), which provides more realistic soil moisture, surface temperature, and sensible and latent heat fluxes. The analysis was based on simulations in domain D04 with a grid spacing of 1 km.

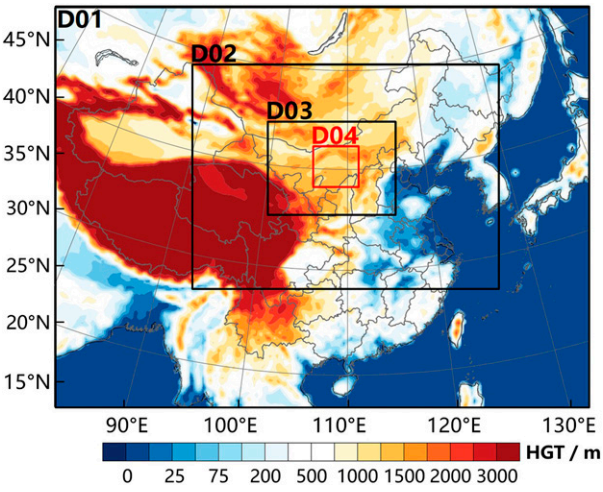

FIG. 2. Terrain height (m MSL) and locations of the various WRF simulation domains.

3. Case overview

a. *Evolution of the boundary and associated convection initiation*

A boundary, which appeared as a weak fine line in the composite radar reflectivity field produced using the lowest two elevation angles of the radar at the LHRD location, formed along the western edge of the Kubchi Desert (denoted by the dashed red circle in Fig. 3a) at ~500 m AGL parallel to the border of the irrigated area and Kubchi Desert at 0818 LST 4 June 2013. The boundary widened slowly from 0900 to 1000 LST at the formation stage and then remained nearly the same (the solid black line in Fig. 4), which was determined by the width of the widest area where the composite radar reflectivities of the lowest two elevations were larger than 0 dBZ at each time during the life cycle of the boundary. The depth of the boundary continued to rise (orange bars in Fig. 4), while the boundary extended northeastward along the oasis–desert interface (Fig. 3c). A sudden rise at the top of the observed boundary at approximately 0930 LST and failure to reach the ground at the bottom were possibly attributable to the radar elevation angle limitation. The boundary became the longest (Fig. 3c) along the edge of the Kubchi Desert at 1358 LST, which occurred ~1 h after the largest difference in ground temperature between the desert and irrigated areas (Fig. 4). Immediately to the east side of the boundary, three cells were initiated almost simultaneously at 1518 LST (Fig. 3e), when the boundary became the deepest (Fig. 4). Subsequently, eight other cells were gradually initiated over the next 70 min under the influence of the boundary (Fig. 3g). Then, all 11 cells established a mesoscale convection system that was approximately parallel to the boundary and moved southeastward.

b. *Synoptic environment*

This CI process occurred in front of a middle-level shortwave trough with low-level southerly wind transporting moisture

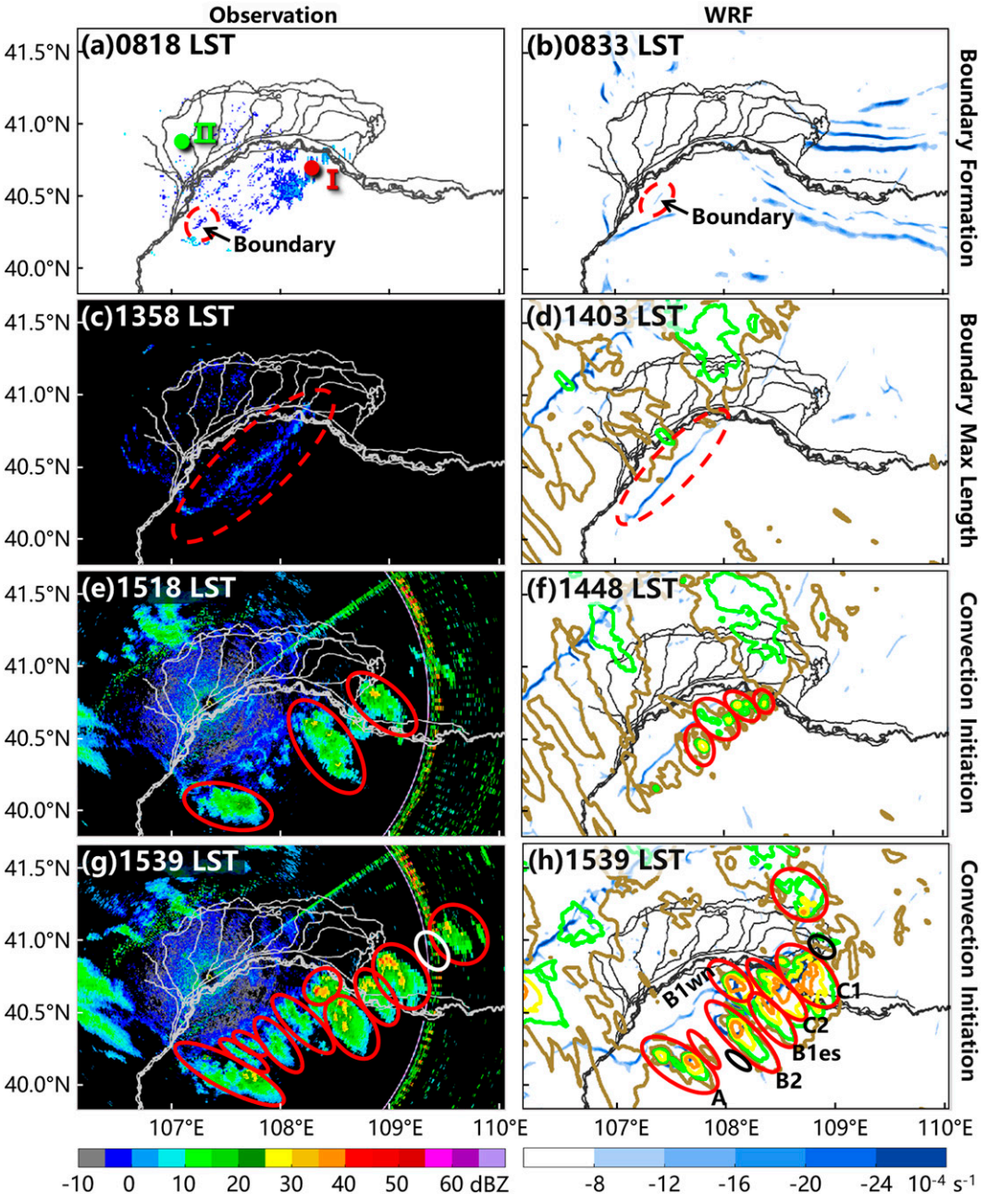

FIG. 3. Composite reflectivities observed by (a),(c),(e),(g) the LHRD radar (shading) and (b),(d),(f),(h) in the WRF simulation (contoured in khaki, green, yellow, and orange for 10, 20, 30, and 40 dBZ, respectively). The data in (a) and (c) are based on the two lowest elevation angles, while (e) and (g) are based on all nine elevation angles. The simulated divergence of wind in the bottom model layer is shaded in blue in (b), (d), (f), and (h) to denote the simulated boundary. The cells with a white circle in (g) and black circles in (h), which have not yet formed at the moment, are also shown to provide a complete picture. Cells with IDs in (h) were adopted in the subsequent trajectory analysis. The red and green points in (a) are the two surface weather stations used to examine the surface temperature differences between the oasis and desert areas, as shown in Fig. 4.

to the Hetao area. At 500 hPa, the Hetao area was dominated by westerly winds with a shortwave trough approaching the irrigated area from the west (Fig. 5a; Fig. 5b shows an enlarged plot of the gray box in Fig. 5a). A weakening cold vortex was located in northeastern China (denoted by C in Fig. 5a). The axis of the subtropical high was located at approximately 20°N in South China Sea (not shown). At 800 hPa (Fig. 5e), the Hetao area was controlled by large-scale southerly winds with low pressure systems to the southwest (L1 in Fig. 5e) and northwest (L2 in Fig. 5e) of the irrigated area and a high

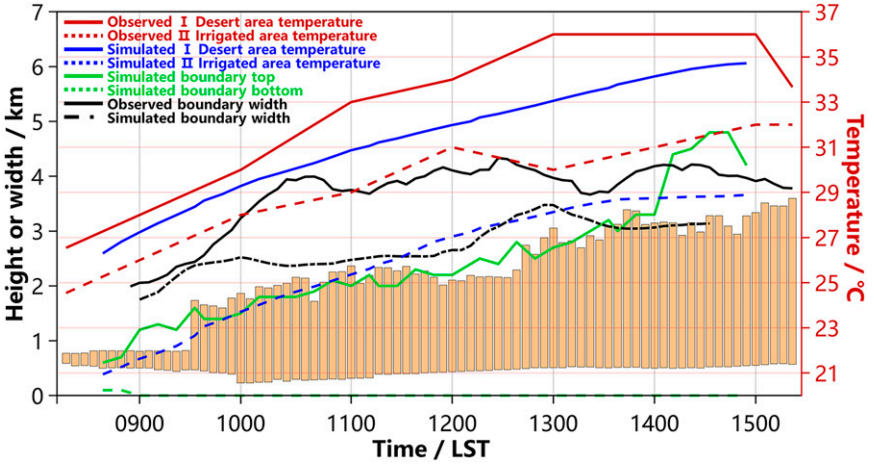

FIG. 4. Evolution of the top and bottom heights of the observed boundary (km AGL, orange bars), observed boundary width (solid black line, *y* axis on the left, with a moving average over 45 min) and surface temperature (°C, red lines) at the oasis and desert stations depicted in Fig. 3a. Additionally, the simulated boundary top and bottom height (km AGL, the base in the dashed green line and the top in the solid green line), simulated boundary width (km, the dash–dotted black line, *y* axis on the left, with a moving average over 45 min) and simulated surface temperature at the same locations as those of the observations (°C, blue lines) are shown.

pressure system (H in Fig. 5e) over the East China Sea. Southerly flow along the western edge of the high pressure system transported abundant moisture to North China (green shading in Figs. 5e,f), producing a high mixed-layer CAPE (MLCAPE) considering entrainment and virtual temperature correction (orange shading in Figs. 5a,b). This case was typical of the most frequent synoptic pattern T1 in Huang et al. (2022), which was favorable for the formation of a surface-driven boundary and CI. This pattern was characterized by a high pressure ridge at 500 hPa over the oasis and an anticyclonic circulation at 700 hPa southeast of the oasis, facilitating southerly winds.

The MLCAPE in the irrigated area was approximately 600 J kg^{-1}, while the MLCAPE in the semiarid area was much lower than that in the humid area (Figs. 5a,b). Skew *T*–log*p* data obtained from the ERA5 data at the location of the LHRD site in the irrigated area at approximately 1 h prior to CI indicated an MLCAPE of ~500 J kg^{-1} (Fig. 6a; the location is indicated with a white cross in Fig. 5b), while skew *T*–log*p* data at the CI location in the desert area indicated an MLCAPE of 96 J kg^{-1} (Fig. 6c; the location is marked with a black cross in Fig. 5b).

The CI location exhibited a much lower MLCAPE; however, its wind profile was more favorable for CI. At both station locations, winds changed from low-level southwesterly winds to middle-level westerly and high-level northwesterly winds (Figs. 6a,c), which indicated warm air advection that was beneficial for the development of deep convection (Davies-Jones et al. 2001; Doswell 2005; Rotunno and Klemp 1982). The wind below 850 hPa at the CI location was much stronger (9 versus 2.5 m s^{-1}) with a larger southerly component than that at the LHRD location, with consistent wind changes with height. However, the wind at the LHRD site exhibited a backing wind change up to ~750 hPa and a veering wind change above that. This complicated real-world environmental wind was different from the uniform background wind in idealized simulations (Lee et al. 2019).

c. *Model validation for the environment*

Overall, the large-scale synoptic situation reproduced in the simulation was similar to that based on the ERA5 data. Both the weakening northeast cold vortex and the shortwave trough at 500 hPa were suitably captured (Fig. 5c). The 800-hPa low pressure system to the southwest and northwest and the high pressure system to the southeast of the Hetao area were also close to those in the reanalysis data (Fig. 5g). The observed southerly flow and associated moisture were also simulated well, except that the simulated moisture near the Hetao area was slightly more widespread.

Due to higher near-surface moisture and lower PBL height, the simulated MLCAPE was higher than that indicated by the ERA5 data at both the LHRD site in the irrigated area and the CI location in the desert area. The simulated MLCAPE in the irrigated area reached 1000+ J kg^{-1} (Fig. 5d). The simulated skew *T*–log*p* data at the location of the LHRD site indicated an MLCAPE of 1078 J kg^{-1} (Fig. 6b; the location is indicated with a white cross in Fig. 5d) and an MLCAPE of 649 J kg^{-1} over the desert area (Fig. 6d; the location is indicated with a black cross in Fig. 5d), which were both higher than the corresponding ERA5 values. The observed low-level southwesterly wind, middle-level westerly wind and high-level northwesterly wind were satisfactorily reproduced at both sites except that the wind at approximately 700 hPa was slightly weaker (Figs. 6b,d). The simulated hodograph at the LHRD site indicated a more apparent backing below 750 hPa (Fig. 6b). The coherent veering wind at the CI

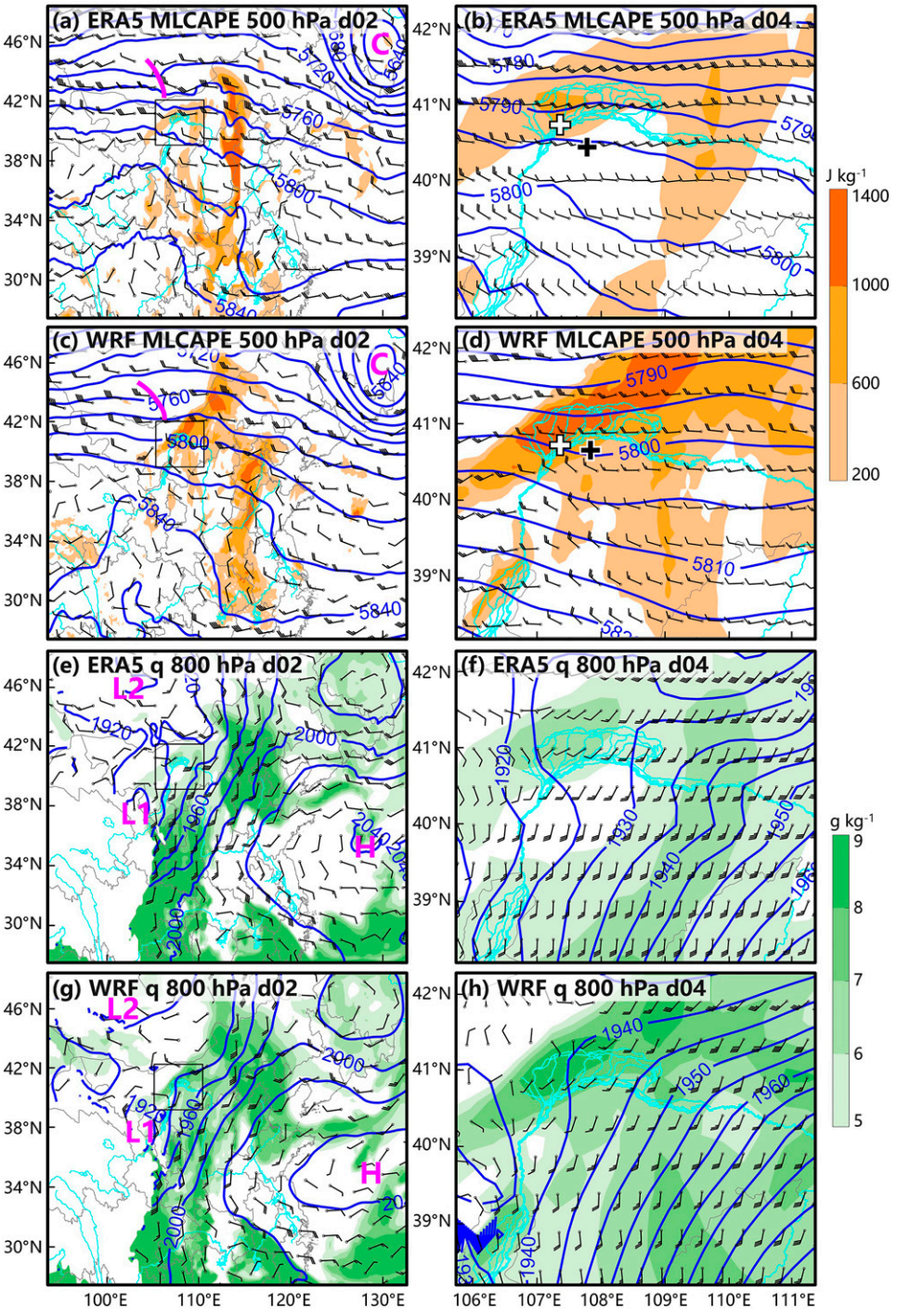

FIG. 5. Synoptic environment based on ERA5 data at (a) 500 and (e) 800 hPa at 1400 LST 4 Jun in (a),(e) d02 with (b),(f) a zoomed-in d04 region (the gray box in the left panels) shown, including the geopotential height (contoured in blue, every 20 gpm), horizontal wind (a full bar denotes 4 m s^{-1}; a half bar denotes 2 m s^{-1}), MLCAPE [J kg^{-1}, shading in (a)–(d)], and water vapor mixing ratio at 800 hPa [g kg^{-1}, shading in (e)–(h)]. The short magenta curve in (a) denotes a shortwave trough. The magenta C, L, and H labels denote the locations of the cold vortex and low and high pressure systems, respectively. (c),(d) and (g),(h) As in (a),(b) and (e),(f), but for the WRF simulation with intervals of 5 gpm for the geopotential height. The white and black crosses in (b) and (d) denote the locations of the LHRD radar site and first CI, respectively, where radiosonde data are shown in Fig. 6. The Yellow River is marked with the cyan line.

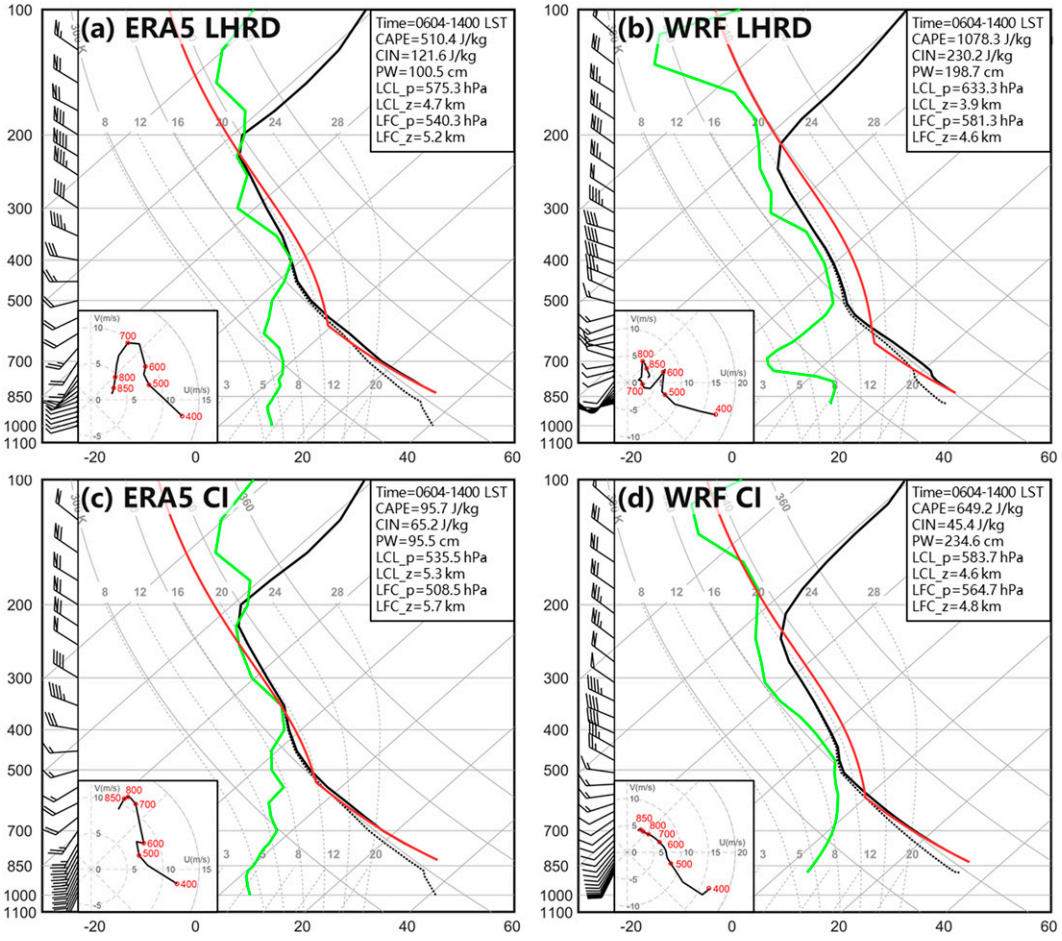

FIG. 6. Skew T–log$p$ data from (a),(c) ERA5 and (b),(d) simulation at the location of the LHRD radar site (top) in the irrigated area and (bottom) the first CI in the desert area at 1400 LST 4 Jun. Parcels are lifted from the mixing layer (red lines). Dewpoint temperature profiles of the environment are indicated with green lines, and ambient temperature profiles before and after virtual temperature correction are denoted with dotted black lines and solid black lines, respectively. Wind barbs (a full bar denotes 4 m s^{-1}; a half bar denotes 2 m s^{-1}) at different levels are shown on the left side of each panel. MLCAPE (J kg^{-1}), convective inhibition (CIN, J kg^{-1}), precipitation water (PW, cm), LCL (km MSL), and LFC (km MSL) of the parcels are displayed in the upper-right corner. Corresponding hodograph diagrams are shown in the lower-left corner, where the winds at specific pressure levels are denoted with red circles.

location (Fig. 6d) was close to that indicated by the ERA5 data (Fig. 6c).

The modeled features of the soil and vegetation distribution were also similar to those based on the MODIS and ERA5 data. The vegetation index, which was described in terms of the albedo (Betts 2000; Tian et al. 2014), was consistent with that based on the MODIS data, with higher values in the irrigated area than in the desert area (Figs. 1a,b). The vegetation index in the irrigated area was higher in the west than in the east. Similar to the reanalysis data, the simulated soil moisture within 1 cm from the ground (Fig. 7b) clearly revealed a lower humidity in the UlanBuh Desert and Kubchi Desert and a higher humidity in the irrigated area, Ordos Plateau and Yellow River passing areas, except with an apparently smaller magnitude than that of the humidity values indicated by the reanalysis data (Fig. 7a). Consistent with the distribution of the soil moisture, the soil temperature within the same layer (Figs. 7c,d) was higher in the arid area and lower in the humid area. Similarly, in the irrigated area, a higher vegetation index in the west than in the east resulted in a higher soil moisture and lower soil temperature in the west than in the east.

Closely related to the suitably simulated underlying surface conditions, surface air features were also well captured by the model. The water vapor mixing ratio at 2 m AGL (Figs. 7e,f) indicated an obvious dry area in the Kubchi Desert and surrounding areas. The water vapor mixing ratio was much higher in the irrigated area, especially in the western part, than in the desert area, possibly due to both the vegetation distribution in the irrigated area and the blocking effect of the Lang Mountains. Notably, higher 2-m temperatures were

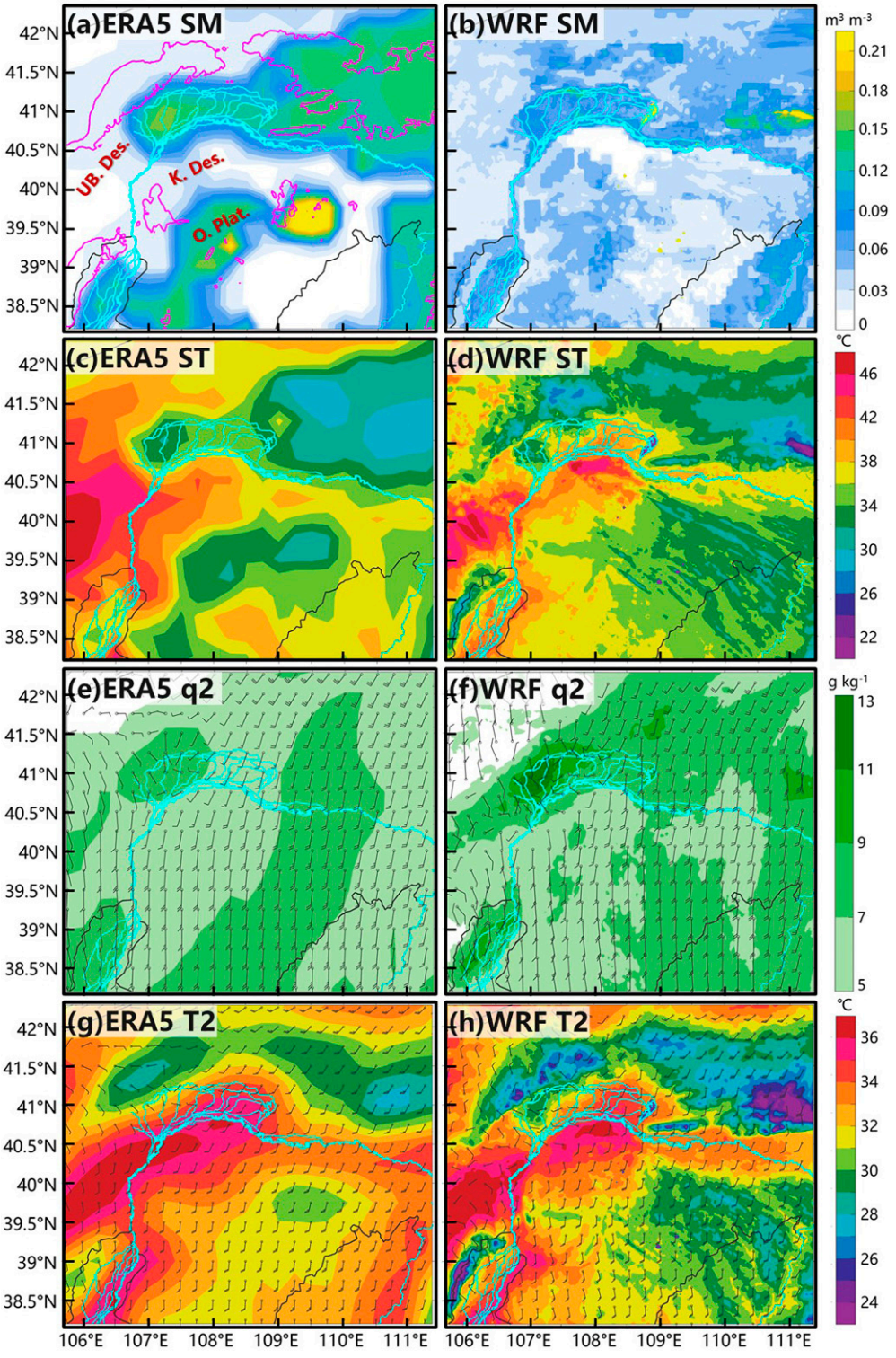

FIG. 7. (a) Soil (within 1 cm below the ground) moisture ($m^3\ m^{-3}$) and (c) soil temperature (°C), as well as (e) surface (2 m AGL) moisture ($g\ kg^{-1}$), (g) surface temperature (°C) and 10-m wind (a full bar denotes 4 $m\ s^{-1}$; a half bar denotes 2 $m\ s^{-1}$) based on ERA5 data at 1400 LST 4 Jun. (b),(d),(f),(h) As in (a),(c),(e),(g), but for the simulation. The Yellow River is represented by the cyan line. The province boundary is represented by black lines. The purple contour in (a) denotes a terrain height of 1500 m MSL. UB. Des., K. Des. and O. Plat. denote the UlanBuh Desert, Kubchi Desert, and Ordos Plateau, respectively.

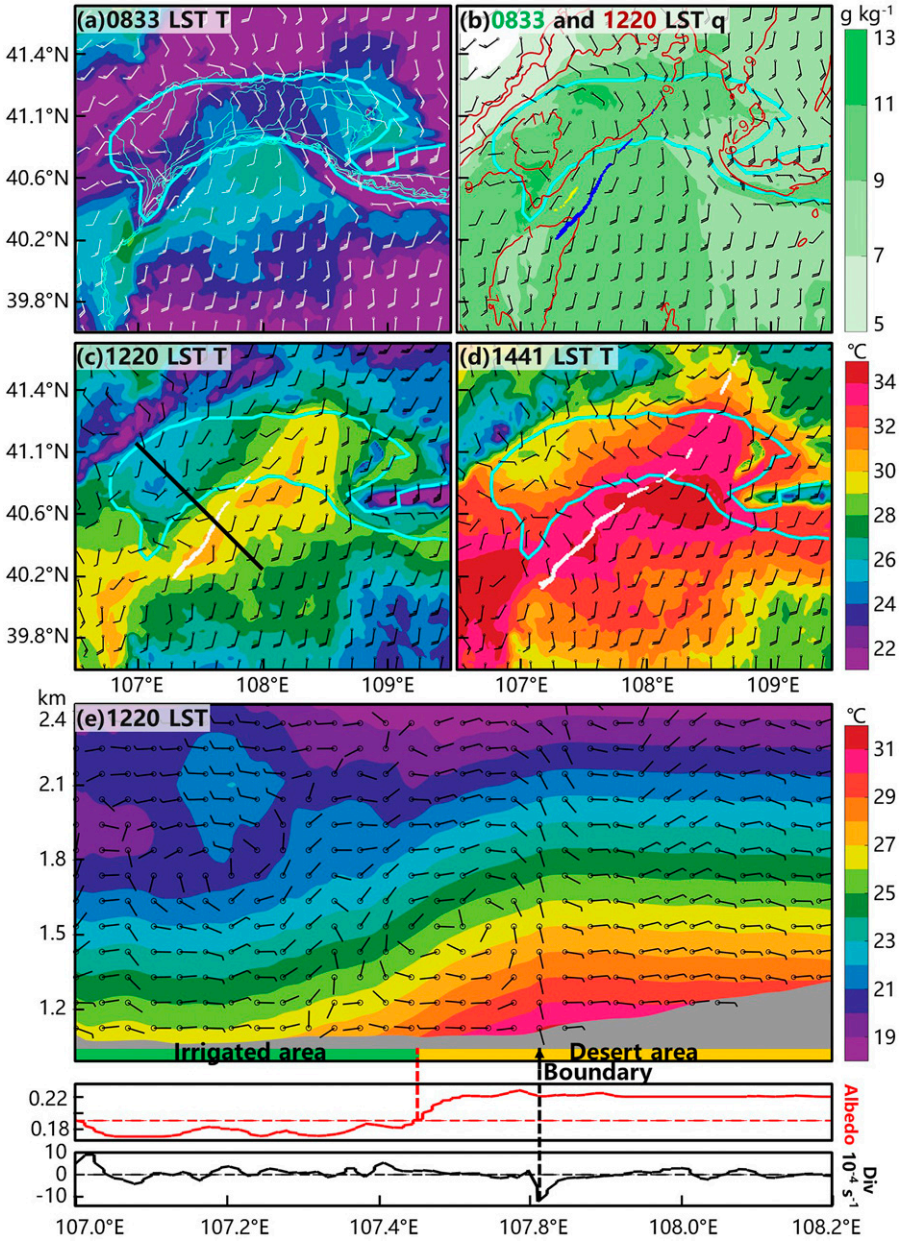

FIG. 8. Simulated temperature (°C, shading), wind (a full bar denotes 4 m s^{-1}; a half bar denotes 2 m s^{-1}), and boundary (white dots) in the bottom model layer at (a) 0833, (c) 1220, and (d) 1441 LST. (b) As in (a),(c), and (d), but for the water vapor mixing ratio (g kg^{-1}, shading) and boundary (yellow dots) at 0833 LST. Additionally, the water vapor mixing ratio (g kg^{-1}, maroon contour) and boundary (blue dots) at 1220 UTC are plotted in (b). The irrigated area is denoted by a cyan contour for albedo values less than 0.19 in (a)–(d). The Yellow River is represented by a thin cyan line in (a). (e) The vertical cross section (km MSL) along the black line in (c), including the temperature (°C, shading) and winds in the plane of the cross section with the original speed (a full bar denotes 4 m s^{-1}; a half bar denotes 2 m s^{-1}) but a direction generated with the original horizontal velocity and 10 times the original vertical velocity. The red line below denotes the surface albedo along the plane of the cross section, with values greater than 0.19 (denoted by the short red dashed line) representing the desert area. The black line denotes the surface divergence along the plane of the cross section, with a value less than 0 (dotted black line) representing convergence, which is used to characterize the position of the boundary.

TABLE 1. Height (km MSL) of the 30-dBZ area, total cloud mixing ratio including liquid water and ice that are larger than 0, LCL, and LFC for parcels lifted from the mixing layer in the CI area at the CI time of cells A, B1es, B1wn, B2, C1, and C2. The ground levels (km MSL) at the CI time of these six cells are given in the last column.

Cell	Height of 30 dBZ (km)	Height of total cloud mixing ratio > 0 (km)	LCL (km)	LFC (km)	Ground level at CI time (km)
A	7.75–8.15	5.10–9.50	5.05	5.30	1.29
B1es	7.20–7.65	6.15–9.40	4.85	5.09	1.09
B1wn	6.75–6.90	4.80–8.60	4.69	4.71	1.06
B2	7.25–8.15	4.95–9.40	4.74	4.83	1.14
C1	7.85–8.15	4.90–10.00	4.87	5.10	1.03
C2	7.70–8.55	4.90–10.50	4.85	5.01	1.04

observed in the desert area than in the irrigated area (Figs. 7g,h), and obviously lower temperatures were observed in the west than in the east in the irrigated area, likely resulting from the higher soil temperature and warm advection due to the southerly wind originating from the arid area. The temperature over the Kubchi Desert and eastern side of the irrigated area produced a southwest–northeast-oriented high-temperature band. While WRF and ERA5 differed in absolute values for MLCAPE (Figs. 5a–d), soil and surface moisture and temperature (Figs. 7a–h), the surface patterns and relative relationships over deserts and irrigation were similar.

4. Mechanisms of boundary formation, evolution, and CI

a. Simulations in comparison with observations

Given the suitably simulated underlying surface and atmospheric environment, the simulated formation and evolution processes of the boundary were similar to those revealed by the radar observations. Simulated boundary formation was defined as the time when the length of the boundary with a divergence $< -8 \times 10^{-4}$ s^{-1} reached 10 km for the first time. The width of the simulated boundary was determined by the width of the widest area where the divergence of horizontal wind in the bottom model layer was less than -8×10^{-4} s^{-1} during the life cycle of the simulated boundary, and the top and bottom heights above the ground of the simulated boundary were defined using the extent of the vertical velocity along the boundary greater than 0.1 m s^{-1}. The simulated boundary occurred near the observed location, namely, the western border of the Kubchi Desert and the irrigated area, and it was roughly parallel to the vegetation contrast line (denoted by a dashed red circle in Fig. 3b). The boundary continued to develop northeastward and moved eastward, similar to the observations, reaching the largest length at 1403 LST (Fig. 3d). Similar to the radar observations, the simulated width slowly widened and then remained almost the same (dash–dotted black line in Fig. 4). The simulated top height above the ground of the boundary continuously increased (solid green line in Fig. 4), indicating an ever-increasing ability to lift air parcels.

The simulated convection was initiated in a manner similar to that based on the radar observations. Four convective cells were triggered almost simultaneously at 1448 LST (Fig. 3f), which occurred 30 min prior to the observed CI. Subsequently, four other cells were triggered immediately east of the boundary within 45 min (Fig. 3h). These simulated cells roughly corresponded to the series of cells in the radar observations (Fig. 3g). Furthermore, there were no interactions between neighboring cells at the CI time, similar to the observed processes. Although the formation of certain cells and the sequence of initiation between the cells slightly differed from the observations, the simulation was adequate for use in the examination of the boundary influence on the CI processes.

The successful simulation of the boundary and CI also suggests that the environmental patterns and relative relationships over deserts and irrigation rather than the absolute values are more important for the boundary and CI accuracy in the simulation, considering the different absolute values but similar patterns for MLCAPE (Figs. 5a–d), soil and surface (Figs. 7a–h) moisture and temperature in WRF and ERA5.

b. Formation and evolution mechanism of the boundary

The formation and evolution of the boundary were closely related to the spatial contrast of temperature because of the greater correspondence between the boundary and the spatial contrast of temperature than that of the water vapor mixing

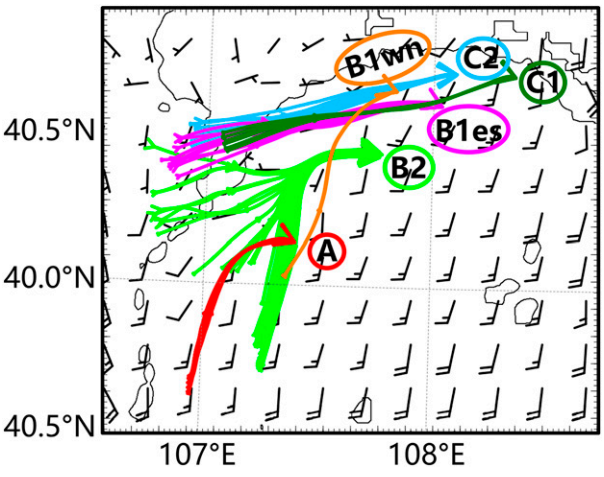

FIG. 9. Backward trajectories of 4 h for the first 30-dBZ parcels in the six examined cells (colored lines). Additionally, the winds (a full bar denotes 5 m s^{-1}; a half bar denotes 2.5 m s^{-1}) in the bottom model layer at 1200 LST are plotted. The irrigated area is denoted by a black contour for albedo values less than 0.19.

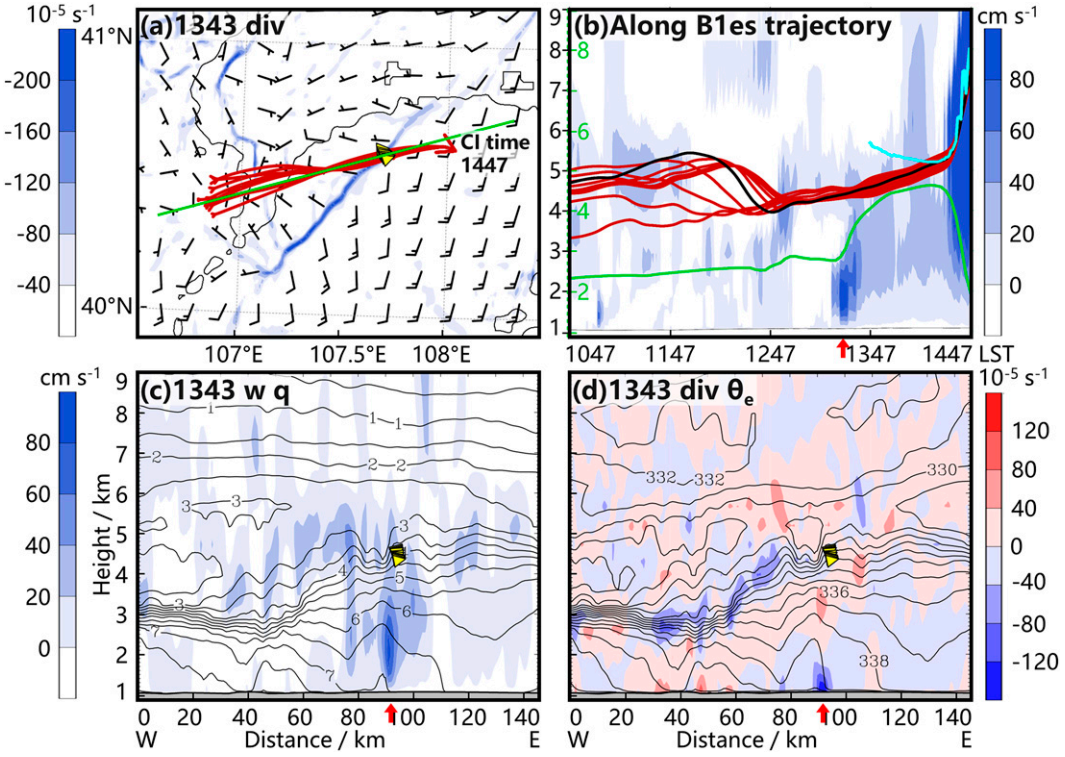

FIG. 10. (a) Backward trajectories of the first 30-dBZ parcels in cell B1es (red lines) in the divergence (10^{-5} s^{-1}, shading) and winds (a full bar denotes 5 m s^{-1}; a half bar denotes 2.5 m s^{-1}) in the bottom model layer at 1343 LST. The yellow triangles along the trajectories denote the positions of the parcels at 1343 LST. The number at the end of the trajectory arrow is the initiation time for cell B1es. The irrigated area is indicated by black contours for albedo < 0.19. (b) Temporal evolution of the trajectory height (km MSL, red and black lines, y axis in black), vertical velocity (cm s^{-1}, shading), LFC for the parcel at its height at the corresponding moment (km MSL, cyan line), and water vapor mixing ratio (g kg^{-1}, green line, y axis in green) along the black trajectory. The location where the parcel along the black trajectory crosses the surface boundary in (b) is indicated by a red arrow on the x axis. The trajectory parcel locations (yellow triangles) in the vertical cross section at 1343 LST along the green line given in (a) are plotted with (c) the vertical velocity (cm s^{-1}, shading) and water vapor mixing ratio (g kg^{-1}, black contours) and (d) divergence of the horizontal wind at each level (10^{-5} s^{-1}, shading) and equivalent potential temperature (K, black contours). The red arrow on the x axis in (c) and (d) denotes the boundary position at 1343 LST.

ratio, as indicated by the simulations. The boundary formed along the isotherm in the high temperature gradient area (white dots and shading in Fig. 8a) rather than along that of the moisture (yellow dots and shading in Fig. 8b) and moved toward the highest temperature over the Kubchi Desert, causing an eastward movement (Figs. 8a,c,d). Similar to the formation stage, the boundary also exhibited a better association with the gradient of temperature than that of the moisture at 1220 LST (blue dots and maroon contour in Fig. 8b). The vertical profile at 1220 LST along the black line in Fig. 8c indicated that an updraft branch occurred in the desert with a higher temperature and a downdraft branch occurred in the irrigated area with a lower temperature, thus forming mesoscale thermal circulation (Fig. 8e). The oasis breeze in the thermal circulation converged with the surface southerly background wind to form the boundary (Figs. 8c,e).

The evolution process of the boundary was mainly affected by the mesoscale thermal circulation at the earlier stage and both thermal circulation and the westerly shortwave trough thereafter. The surface temperature over the desert area (red point in Fig. 3a) was higher than that over the irrigated area (green point in Fig. 3a) from the boundary formation stage to CI in both observations and simulations (red and blue lines in Fig. 4). The increase in the temperature difference between the desert and irrigated areas supported the general increase in the depth of the boundary, similar to sea-breeze circulation (Markowski and Richardson 2011). The approaching shortwave trough also strengthened the boundary after 1220 LST by intensified convergence. Our numerical simulations revealed that the approaching shortwave trough caused an enhancement in the northerly wind and thus a stronger convergence with the southerly flow (not shown).

c. *Impact of the boundary on CI*

To study the specific impact mechanism of the boundary on CI processes, six noninteracting cells (including A, B1wn, B1es, B2, C1, and C2; IDs are marked in Fig. 3h) were selected to perform backward trajectory analyses for 4 h using the 3-min-resolution

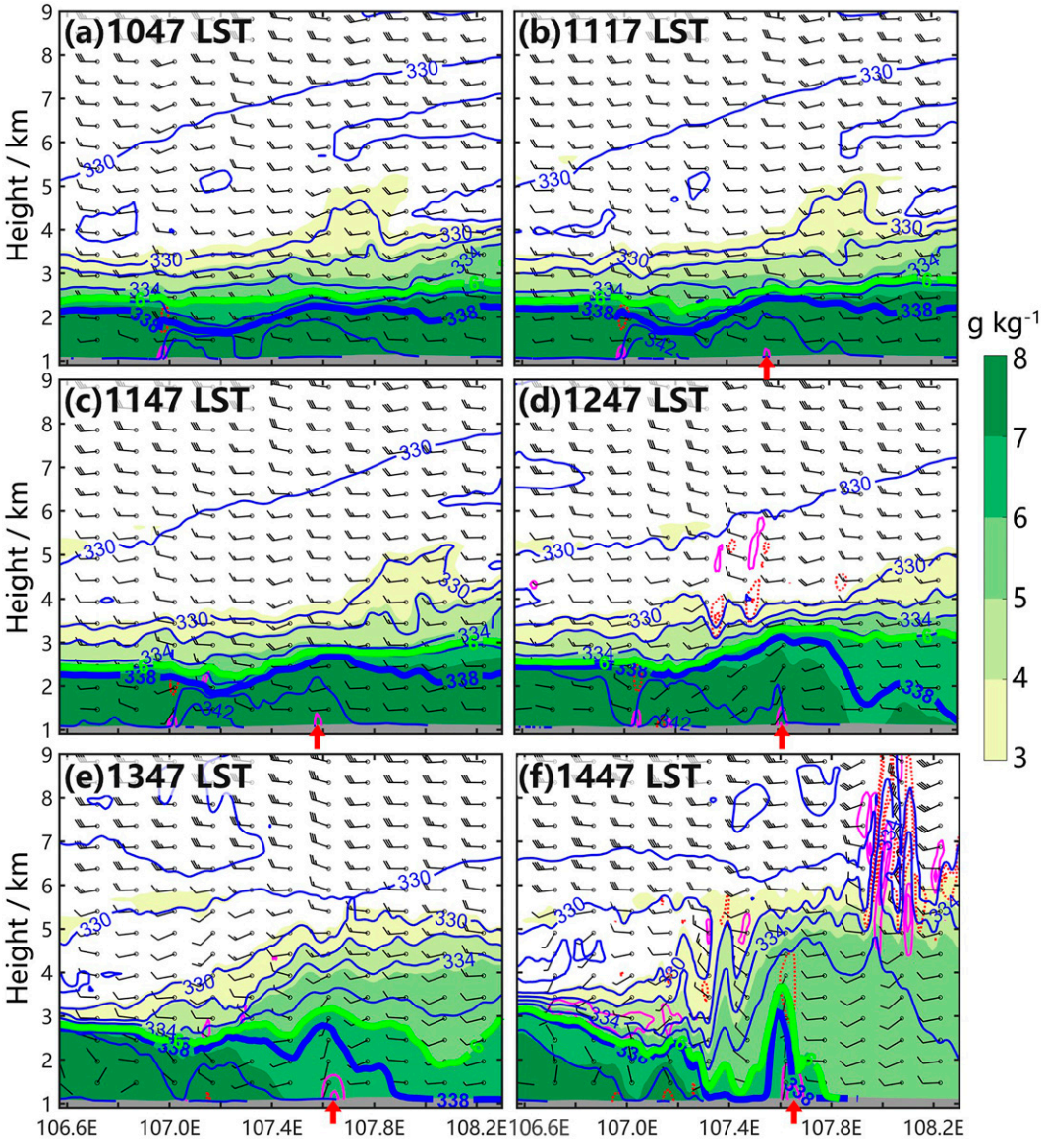

FIG. 11. Time evolution of vertical cross sections (km MSL) along the green line in Fig. 10a of flow (winds with the original speed but a direction generated with the original horizontal velocity and 10 times the original vertical velocity, a full bar denotes 4 m s^{-1} and a half bar denotes 2 m s^{-1}), moisture (water vapor mixing ratio, g kg^{-1}, shading), and equivalent potential temperature (K, blue lines) for Cell B1es at (a) 1047, (b) 1117, (c) 1147, (d) 1247, (e) 1347, and (f) 1447 LST. The 6 g kg^{-1} water vapor mixing ratio and 338-K equivalent potential temperature are highlighted by bold green and blue lines, respectively. The boundary is indicated by solid magenta lines of -8, -16×10^{-4} s^{-1} divergence at low levels and dotted red lines of 8×10^{-4} s^{-1} divergence at middle levels at approximately 107.6°E and denoted by red arrows on the x axis.

model output in 30-s calculation intervals of the air parcels issued from where reflectivities first reached 30 dBZ (vertical location is given in the second column in Table 1) by RIP4 (for Read, Interpolate and Plot), which is a FORTRAN-based program that allows users to obtain graphical output from the WRF model. Each parcel was released at 0.05-km vertical intervals and 1-km horizontal intervals within the area where the reflectivity was higher than 30 dBZ at the initiation time. The heights above mean sea level of the 30-dBZ area, cloud area, LCL, and LFC for parcels lifted from the mixing layer and ground level at the CI location at the CI time of the six examined cells are given in Table 1.

The different cells had different sources of parcels even though these cells were all initiated through the same boundary lifting. According to the horizontal distribution of the backward trajectories over 4 h, the six examined cells could be divided into three categories (Fig. 9): the first 30-dBZ parcels originated from the south–southwest side (hereafter referred to as the southern side, including cells A and B1wn),

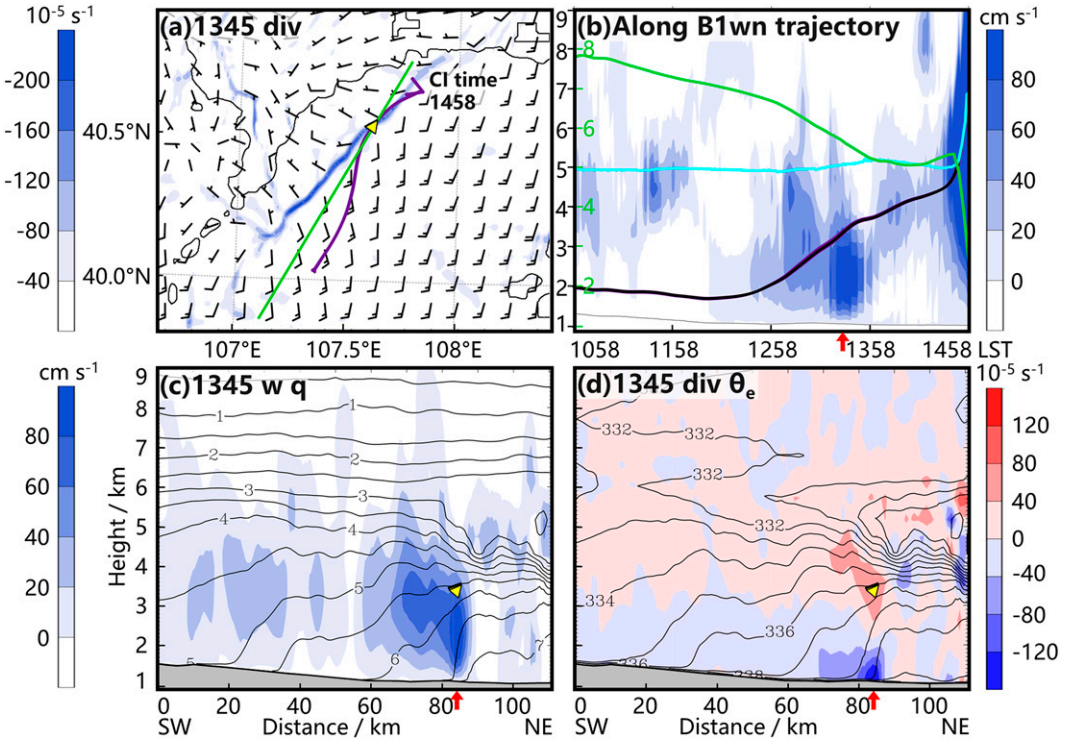

FIG. 12. As in Fig. 10, but for the southerly parcels (purple lines) in cell B1wn at 1345 LST. The location where the parcel along the black trajectory crosses the surface boundary in (b) is shown by a red arrow on the *x* axis. The red arrow on the *x* axis in (c) and (d) denotes the boundary position at 1345 LST.

the west–southwest side (hereafter referred to as the western side, including cells B1es, C1, and C2), and both the southern and western sides (cell B2).

Since the parcels stemming from the same direction exhibited similar characteristics (not shown), we chose cells B1es, B1wn, and B2 to reveal the characteristics of the parcels in the CI region from the western, southern, and both directions, respectively. The trajectories of the parcels in cell B1es covered the cold and wet irrigated area to the west and the dry and hot desert area to the east (Fig. 10a; the yellow triangles denote the positions of the parcels at the time shown in the panel caption, which is 1343 LST here. The same time convention is used for Figs. 12–15). The time–height evolution of these air parcels indicated that the first 30-dBZ parcels all originated from the middle level on the western side over the oasis (Fig. 10b). The cross section roughly along the trajectories of the parcels in Cell B1es (green line in Fig. 10a) revealed that the water vapor mixing ratio and equivalent potential temperature were higher at the boundary (red arrow in Figs. 10c,d and 11) than those in the surroundings, indicating that the boundary converged and transmitted moisture and heat upward at least 3.5 h prior to CI (Fig. 11), which were important for the development of deep moist convection initiation in addition to the thicker unstable layer indicated by the decreasing equivalent potential temperature with height over the desert area. The higher near-surface equivalent potential temperature at the boundary (Figs. 10d and 11) is consistent with the result from Garcia-Carreras et al. (2011). As supported by the evolution of moisture (green line in Fig. 10b) and LFC for the parcel at its height at the corresponding moment (cyan line in Fig. 10b) along one typical air parcel trajectory (black line in Fig. 10b) originating from middle levels, these parcels were close to the LFC before initiation with a high water vapor mixing ratio associated with boundary lifting. When these parcels passed over the boundary, they were slightly raised by weak lifting of the boundary, thereby easily reaching the LFC and achieving initiation. CI did not occur early at approximately 1147 LST even if the parcel occurred higher than at 1437 LST, possibly due to the low water vapor mixing ratio (Fig. 10b). This result indicated that even though a CI occurred over a surface boundary without a near-surface stable layer, the inflow may originate from middle levels rather than in contact with the surface. This feature is different from the common situation where surface-based CI exhibits surface boundaries, and the parcels mainly originate from near the surface, while elevated CI processes usually do not exhibit obvious surface boundaries, and the air parcels largely originate from above the top of the PBL (Wilson and Roberts 2006).

The CI process in cell B1wn revealed a different behavior. The process was first triggered by all the low-level parcels stemming from the south that were strongly lifted as they crossed the boundary (Figs. 12a,b). The parcels exhibited veering horizontal trajectories (Fig. 12a), which resulted in the parcels in cell B1wn passing across the boundary within a longer period than that required by the parcels in cell B1es (Figs. 10a,b). Similar to cell B1es, the water vapor mixing ratio and equivalent

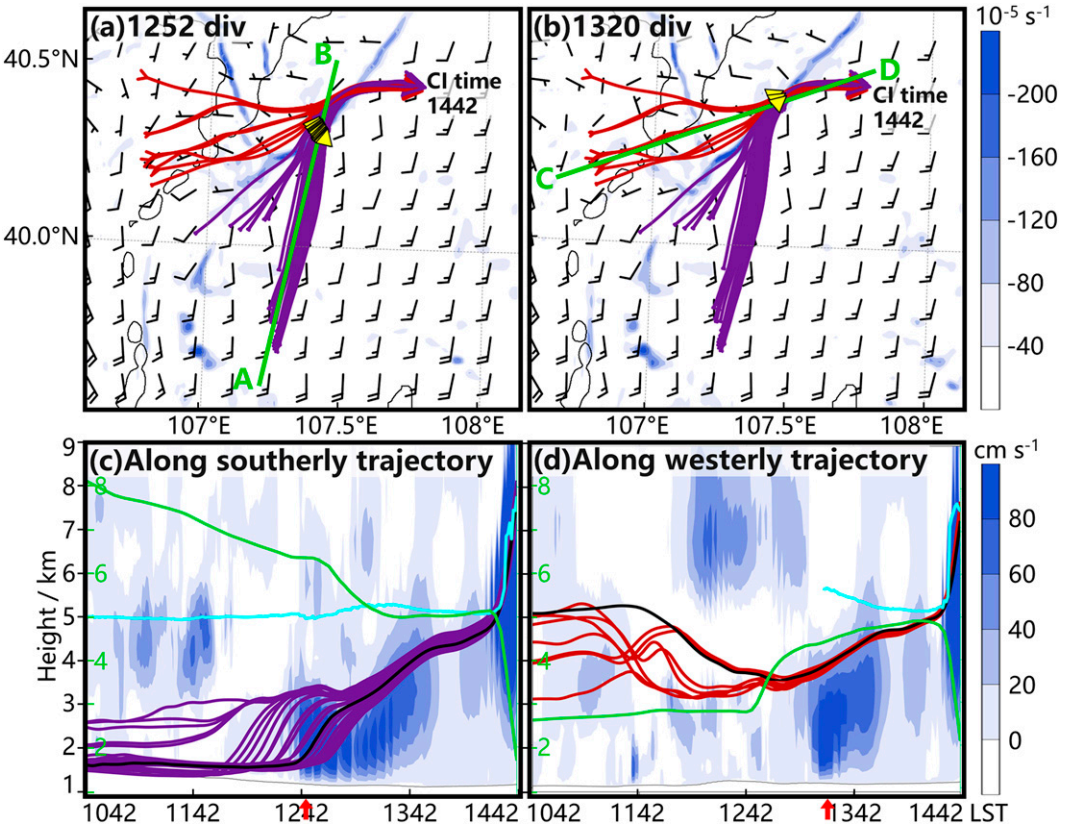

FIG. 13. As in Figs. 10a and 10b, but for the southerly parcels in cell B2 along line AB shown in (a) at 1252 LST on the left and westerly parcels along line CD shown in (b) at 1320 LST on the right. The location where the parcel along the black trajectory crosses the surface boundary in (c),(d) is shown by a red arrow on the *x* axis.

potential temperature in the environment before initiation were also higher than those in the surroundings at the same level (Figs. 12c,d), which was conducive to CI. Upward transport of moisture and heat flux by the boundary also obviously occurred. Although the water vapor mixing ratio decreased over time as the parcel moved northward, the water vapor mixing ratio remained high enough for CI (Fig. 12b).

The parcels that first reached 30 dB*Z* in cell B2 originated from both the south and west. The veering horizontal distribution of the southern parcel trajectories was similar to that of the parcel trajectories in cell B1wn, while the horizontal distribution of the western parcel trajectories was similar to that of the parcel trajectories in cell B1es (Figs. 13a,b). The air parcels on the southern side all stemmed from the low levels, while the parcels on the western side all stemmed from the middle levels, which was consistent with the results obtained based on cells B1wn and B1es. Namely, the southern parcels were subject to longer and stronger boundary uplifting than were the western parcels (Figs. 13c,d).

To understand why the parcels transported by the oasis breeze of the mesoscale thermal circulation from the low-level west were not lifted to their LFCs by the boundary, 4-h forward trajectories from 1200 to 1600 LST of the western low-level parcels were obtained at 49 horizontal positions (magenta dots in Fig. 14a). At each horizontal position, parcels were released at height intervals of 0.1 km within the layer from 1 to 2.2 km above mean sea level. A series of the most representative parcels from the low-level west (LLW) are shown in Fig. 14 and indicate that the parcels below 1.2 km (red and black lines in Figs. 14a,b) were advected by the oasis breeze toward the east and uplifted by the boundary to approximately 3 km. However, these 3-km parcels moved slightly slower than the boundary, as indicated by the yellow triangles behind the boundary along the red trajectories (Fig. 14a), preventing them from being continuously uplifted to reach the LFC (Fig. 14b). In contrast, the parcels above 1.2 km (orange lines) moved mainly northward or northeastward and thus were barely affected by the boundary. Among the 49 horizontal positions, the low-level parcels at 4 positions reached the LFC (not shown), but these parcels were all lifted by the gust front of the previously initiated convection rather than by the boundary. This result suggests that a short lifting time was likely the main reason that the western low-level parcels were not those that first reached 30-dB*Z* area.

The vertical velocities along the trajectories further confirmed the major role of the lifting time. The vertical velocities of the western low-level parcels (approximately 120 cm s^{-1}; the red lines in Fig. 14f) were similar to those of the southern low-level parcels (80–150 cm s^{-1}; purple lines in Figs. 14d,e). However, the uplift duration of the western low-level parcels

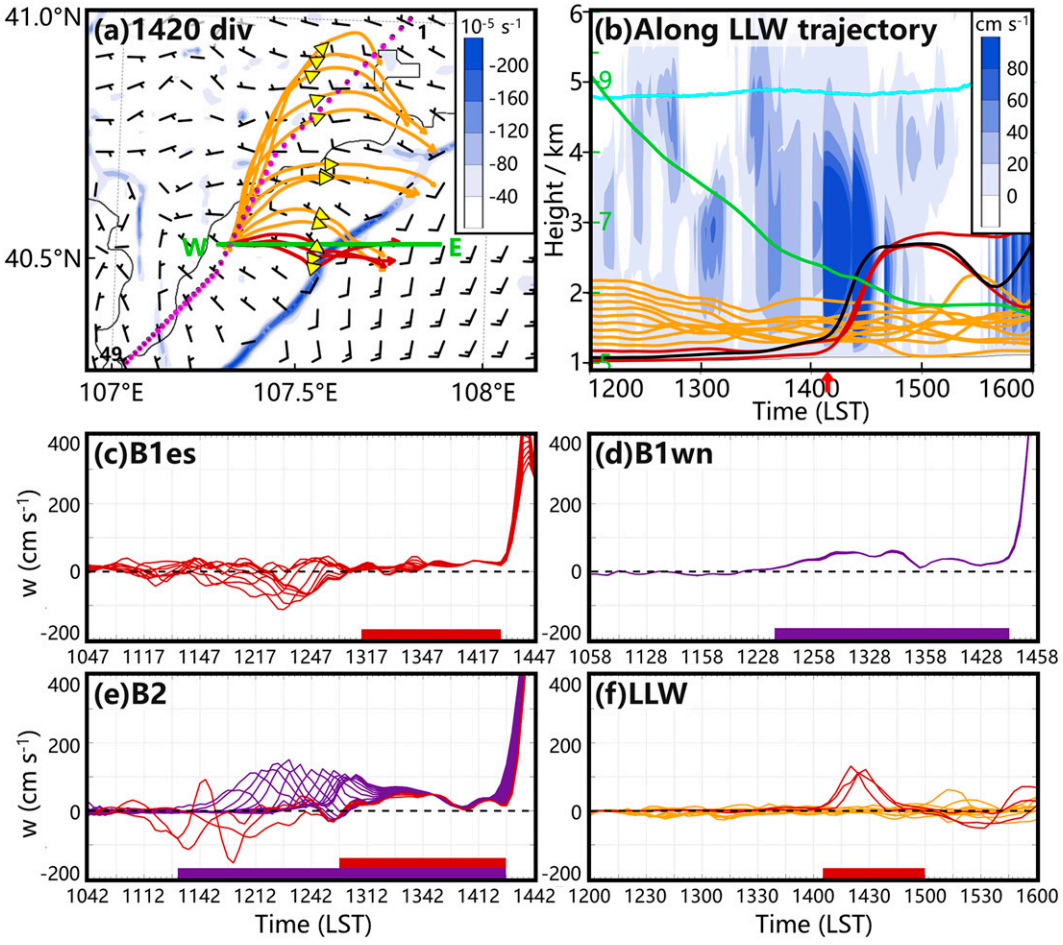

FIG. 14. (a),(b) As in Figs. 10a and 10b, but for the forward trajectories from LLW released at the different levels at one of the 49 magenta dots along line WE shown in (a) at 1420 LST. The location where the parcel along the black trajectory crosses the surface boundary in panels (b) is shown by a red arrow on the *x* axis. (c)–(f) The evolution of the vertical velocity (cm s^{-1}) along the parcel trajectories of cells (c) B1es, (d) B1wn, (e) B2, and (f) from LLW with their respective durations of boundary uplift (the rectangles on the *x* axis in corresponding colors).

reached only approximately 45 min (red rectangle on the *x* axis of Fig. 14f), which was significantly shorter than that of the southern low-level parcels (approximately 120 min for cell B1wn and approximately 180 min for cell B2; purple rectangles in Figs. 14d,e).

The differences in the uplift duration between the western and southern parcels by the boundary were related to changes in the environmental wind direction at the different levels (Fig. 15). Parcels in a flow that blows away from the boundary might be advected by the flow away from the boundary, while parcels in a flow that blow toward the boundary might be advected toward the boundary. Regarding the southern parcels (Fig. 15b), the wind profile with the southerly wind at the surface, the southwesterly wind at 700 hPa and the westerly wind at 600 hPa advected the low-level parcels moving toward the boundary below 710 hPa, then remained nearly parallel to the boundary and slowed above 710 hPa. After the velocity perpendicular to the boundary was reduced to 0, the parcels started to wrap around in space above the boundary (low-level southerly trajectories in Fig. 15f, projected onto the cross section perpendicular to the boundary at 1400 LST along the black line shown in Fig. 15d), which resulted in a longer uplift time for these parcels (at least 2 h from 1200 to 1400 LST in Fig. 15f) and therefore higher probabilities of reaching the LFC. However, the southern middle-level parcels could barely reach the area above the boundary. These parcels moved away from the boundary because the southern side of the boundary at 700 hPa was mainly dominated by the west–southwesterly wind diverging from the boundary (dashed yellow line in Fig. 15b).

Relative to the southern parcels, the western low-level parcels were advected toward the boundary in the northwesterly oasis breeze in the thermal circulation (Figs. 8a,d, the dotted red line in Fig. 15a). However, with the rising air parcels approaching the boundary, the velocity perpendicular to the boundary of parcels in the south–southwesterly wind at 700 hPa diverging from the boundary was reduced (dotted yellow line in Fig. 15a); thus, parcels lagged behind the boundary and were no

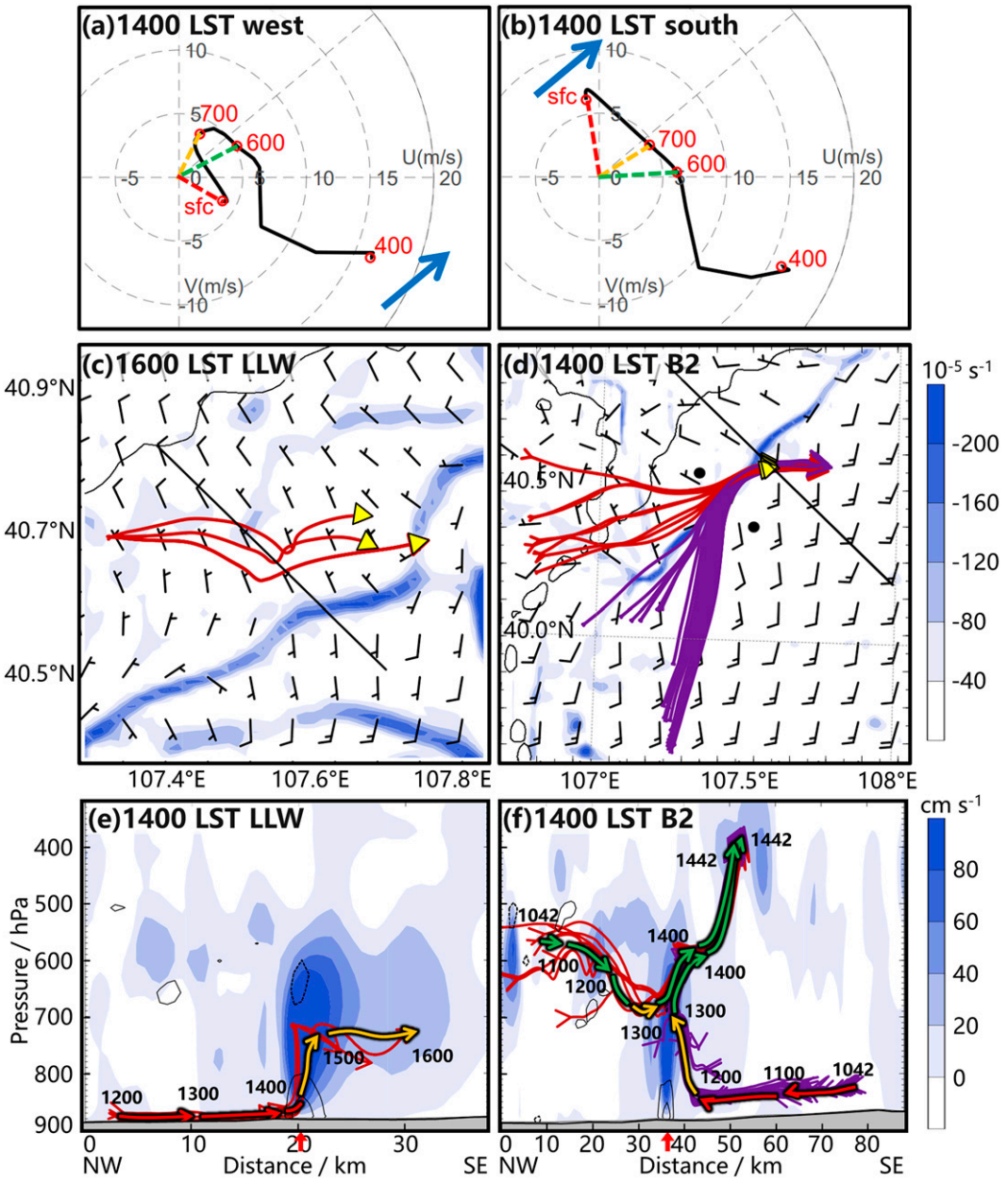

FIG. 15. (a),(b) Hodographs at 1400 LST of the selected places at black dots in (d) on the west and south sides of the boundary. Dashed red, yellow, and green lines indicate the directions of the surface, 700-hPa, and 600-hPa winds. The blue arrow indicates the direction and location of the boundary at 1400 LST relative to the location of the hodograph. (c),(d) Horizontal distribution of trajectories of parcels from LLW at 1600 LST and B2 at 1400 LST. The locations of parcels are indicated by yellow triangles. The divergence (10^{-5} s^{-1}, shading) and winds (a full bar denotes 5 m s^{-1}; a half bar denotes 2.5 m s^{-1}) in the bottom model layer are also shown. (e),(f) The trajectories from LLW and cell B2 projected onto the cross sections along black lines shown in (c) and (d) are indicated by the red hourly arrows at surface, with yellow indicating that below 700 hPa and green indicating that above 700 hPa, which is the same color convention as that shown in (a) and (b). The numbers along the trajectories in (e) and (f) denote the time (LST) when the parcels reach this point. The vertical velocity (cm s^{-1}, shading) and boundary location (red arrow on the x axis) indicated by the convergence (solid black lines of -8, -16×10^{-4} s^{-1} divergence at the low level and dotted black lines of 8×10^{-4} s^{-1} divergence at the middle level) along the cross sections are also shown.

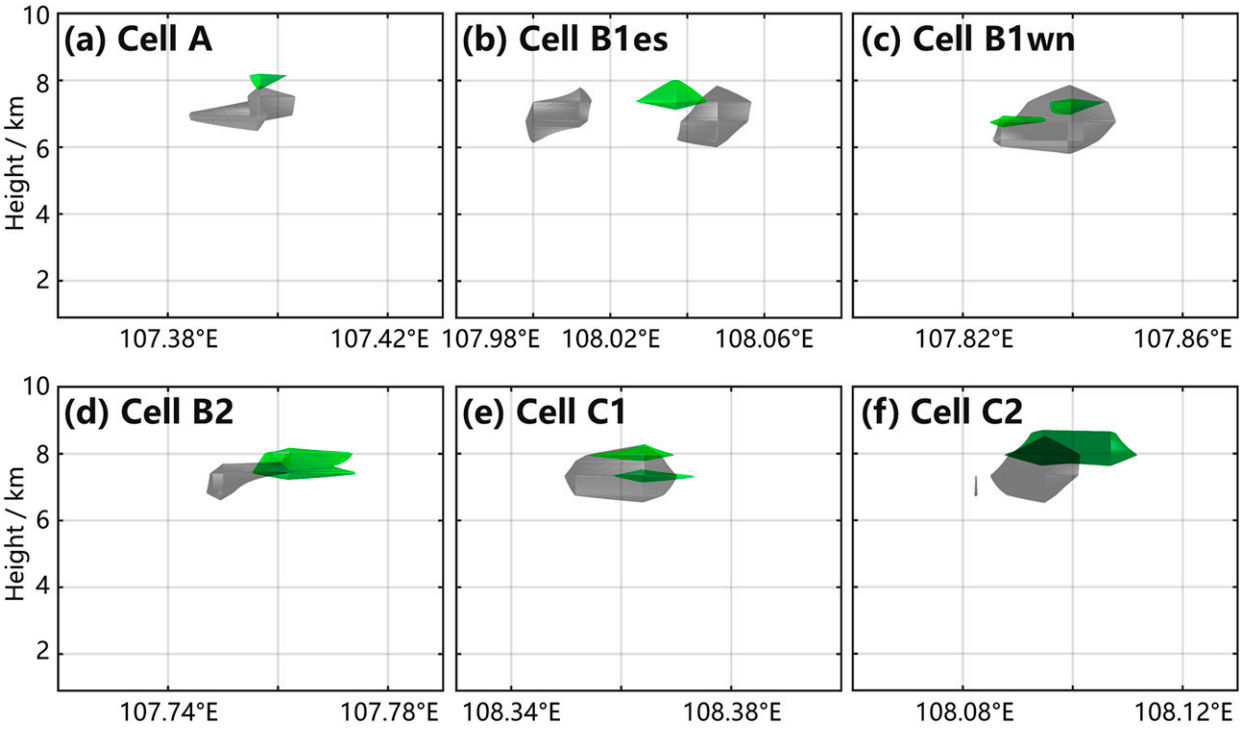

FIG. 16. Three-dimensional isosurfaces of the simulated updraft and reflectivity cores for cells (a) A, (b) B1es, (c) B1wn, (d) B2, (e) C1, and (f) C2 at CI times. The isosurfaces in gray and green denote the top 1% vertical velocity and 30-dBZ reflectivity, respectively. South is out of the plane.

longer uplifted (Fig. 15c). The shorter uplift time (less than 1 h from 1400 to 1500 LST in Fig. 15e) maintained the parcel height at approximately 700 hPa below the LFC and thus failed to produce CI. The feature whereby the parcels were alternately lifted for a short time by the boundary and decelerated by divergence at ~700 hPa immediately west of the boundary (Figs. 15a,e) could have resulted in a jump in the vertical velocity of these air parcels, as shown in Fig. 14b. In contrast, the velocity that was perpendicular to the boundary of the western middle-level parcels was higher than that of the parcels originating at the low levels; the longer hourly distance from 1100 to 1200 LST is shown in Fig. 15f (~11.18 km h^{-1}) for the western middle-level parcels and the shorter hourly distance from 1300 to 1400 LST is shown in Fig. 15e (~8.35 km h^{-1}) for the western low-level parcels. Consequently, even though the western middle-level parcels in the south–southwesterly wind at 700 hPa were also decelerated (yellow arrow in Fig. 15f), these parcels continued to move northeastward at a higher speed than that of the western low-level parcels and thus were lifted for a longer time than parcels from LLW. After reaching the boundary and being uplifted to higher levels, the parcels were quickly transported across the boundary by westerly winds, resulting in a short lifting duration.

In addition to the above trajectory analyses starting from the 30-dBZ reflectivity core, 4-h backward trajectories starting from the updraft core at the CI time for all 6 examined cells were also calculated, as the updraft was the primary engine of convection. Trajectories that started at the updraft core were generally consistent with those that started at the 30-dBZ reflectivity area concerning the effect of the boundary on the CIs. The updraft core of each cell was determined as points with the top 1% vertical velocity (Marion and Trapp 2019) at 1-km horizontal resolutions in a volume with a horizontal area determined by positive vertical velocity at the maximum vertical velocity level in the cell, and the vertical extent was from the surface to 16 km AGL at a 0.05-km interval (Fig. 16). Using the top 1% vertical velocity criterion produced an updraft core with a vertical velocity larger than ~5 m s^{-1}.

Trajectories that began at the updraft cores (Fig. 17) had similar features to those that began at the 30-dBZ reflectivity region (Fig. 9), as all the parcels from the 30-dBZ reflectivity region were closely associated with strong updraft speed at CI time (Fig. 16). The origins were still mainly from the low-level south and middle-level west areas (Fig. 17). The parcel sources of Cells A (low-level south), B2 (both low-level south and middle-level west) and C1 (middle-level west) remained the same. The parcel sources of Cells B1es, B1wn and C2 were mainly the same with dominant middle-level west, low-level south, and middle-level west, respectively, with small amounts of additional origins from low-level south, middle-level west, and low-level south, respectively. In addition, very few parcels were traced back to high-level northwest in Cells B1es and B1wn (Figs. 17b1,b2,c1,c2), which seemed to have been advected into the updraft without obvious influence from the boundary. These results were mainly consistent with the conclusions

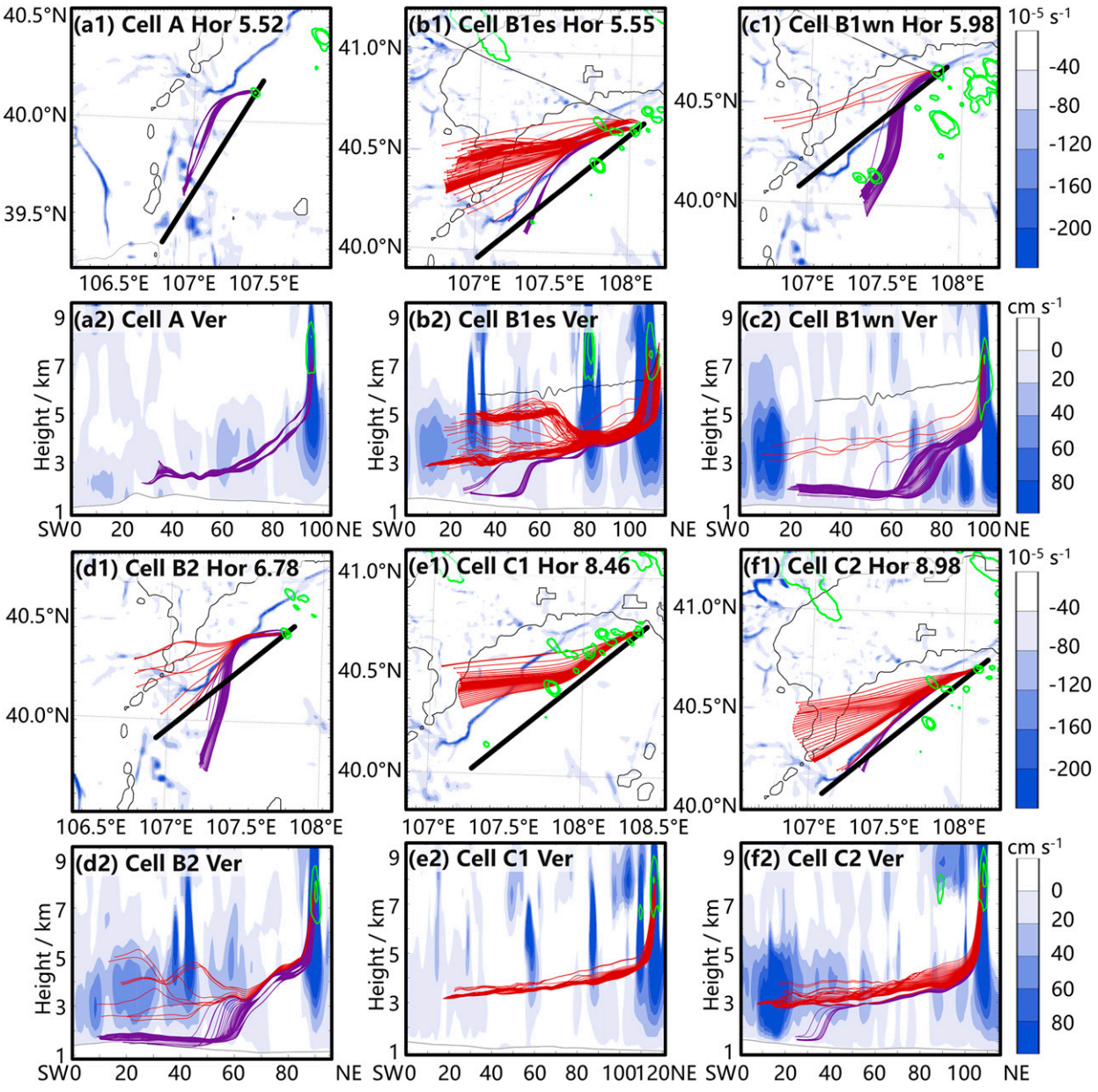

FIG. 17. (a1)–(f1) Horizontal distribution of trajectories (purple lines, red lines, and black lines denote parcels from low-level south, middle-level west, and high-level northwest, respectively) starting from the updraft core (determined using the top 1% vertical velocity) in the six examined cells at CI times. The numbers in their titles are the lowest magnitude of the vertical velocity of the tracked parcels (m s^{-1}). The divergence in the bottom model layer (10^{-5} s^{-1}, shading) and composite reflectivities of 20 and 30 dBZ (green contours) are also shown. The irrigated area is indicated by black contours of albedo < 0.19. (a2)–(f2) The trajectories projected onto the cross sections along black straight lines in (a1)–(f1) are indicated by corresponding lines. The vertical velocity (cm s^{-1}, shading) and reflectivities of 20 and 30 dBZ (green contours) along the cross sections are also shown.

obtained using 30-dBZ reflectivities about the boundary effect on CI.

To provide a big picture of the CI environment of the examined cells, the average distribution of convergence, vertical velocity, CAPE, CIN, and water vapor mixing ratio along the boundary over the CI times of the six cells at 1442 LST (B2), 1445 LST (C2), 1447 LST (B1es), 1448 LST (C1), 1451 LST (A), and 1458 LST (B1wn) are shown in Fig. 18. The radar reflectivities of 20 and 30 dBZ around the CI locations are shown in Fig. 18a, and the positions of each cell marked on the x axis in Fig. 18b are located based on backward trajectory analysis. The results showed that CI occurred under the impacts of both thermal and dynamic environments. With the general small CIN along the boundary, Cell A was triggered mainly

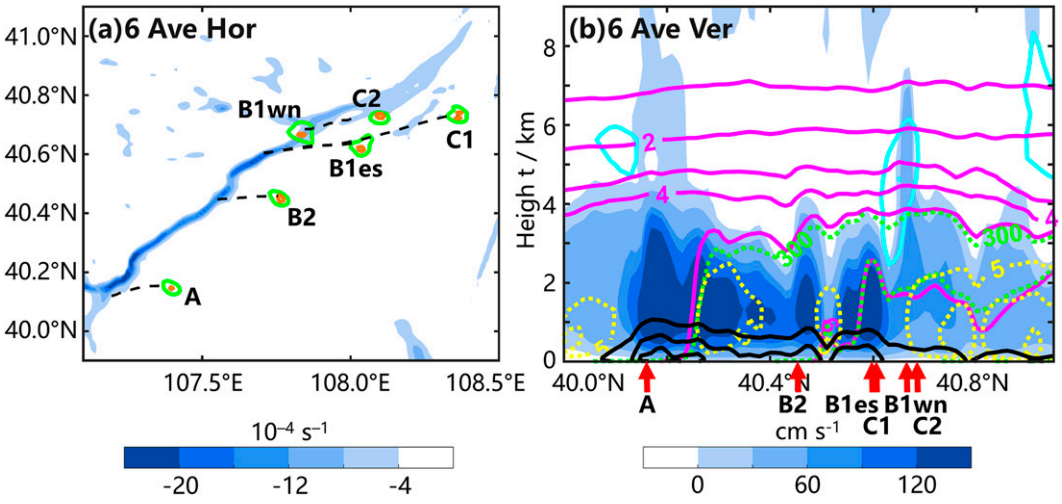

FIG. 18. (a) Horizontal distribution of convergence (10^{-4} s^{-1}, shading, denoting the boundary) averaged over the CI times of the six cells at 1442 (B2), 1445 (C2), 1447 (B1es), 1448 (C1), 1451 (A), and 1458 LST (B1wn). The CI locations of the six cells are given by the radar reflectivities of 20 and 30 dBZ (contoured in green and orange). (b) Average of the vertical cross sections of vertical velocity (cm s^{-1}, shading), divergence (contoured in black for −8, −16, −24 × 10^{-4} s^{-1}), water vapor mixing ratio (g kg^{-1}, contoured in magenta), CAPE (contoured in dotted green lines for 300, 600, and 900 J kg^{-1}), CIN (contoured in dotted yellow lines for 5, 10, and 15 J kg^{-1}), and reflectivities (contoured in cyan for 10, 20, and 30 dBZ) along the boundary by taking a point every 2 km in the latitudinal direction at the CI times of each cell. The positions of the six cells marked by red arrows on the x axis were located through backward trajectory analysis, as shown by the dashed black lines in (a).

due to intense surface convergence and strong updraft, while other cells were triggered with both strong or deep updraft and larger moisture and CAPE. The six cells tended to be triggered where the surface convergence was more intense or the updraft was deeper than in the surrounding areas (Fig. 18b). Overall, the CI was essentially the result of the interaction between the synoptic conditions, which had westerly winds at middle levels and southerly winds at low levels providing instability and moisture, with a surface-driven boundary providing uplift at low to middle levels.

5. Summary and discussion

This study investigated the formation and evolution of a boundary layer convergence line and related CI processes occurring on 4 June 2013 in the Hetao area in northern China, where highly heterogeneous vegetation often forms boundaries parallel to the dominant vegetation contrast line across the interface between the oasis and desert areas. These boundaries occasionally initiate convection, which may intensify downstream and cause severe disasters (Yu 2012; Meng et al. 2013). In this case, a series of cells were triggered along the boundary without affecting each other within 70 min and finally merged into a quasilinear mesoscale convective system.

CI occurred in a synoptic environment with favorable lifting and moisture supply. A shortwave trough at 500 hPa moved toward the Hetao area from the west. At 850 hPa, a low pressure center was located to the west of the Hetao area, while widespread southerly flows along the west edge of a low-level high pressure system over the East China Sea dominated the Kubchi Desert and its eastern area, transporting moisture northward.

Based on observations and a convection-allowing simulation that suitably reproduced the observed evolution of the boundary, convection, synoptic environment and land surface features, the evolution mechanism of the boundary and associated CI were examined. The results revealed that the evolution of the boundary was related to both the thermal differences between the irrigated area and Kubchi Desert and the background wind. Mesoscale thermal circulation formed across the interface between the oasis and Kubchi Desert areas, where high gradients of soil moisture, latent heat flux, and near-surface air temperature occurred. Along the interface over the Kubchi Desert, a southwest–northeast boundary formed due to the convergence of the oasis breeze branch of the thermal circulation and the near-surface southerly wind. The boundary formed and was enhanced along the isotherm in the high temperature gradient area rather than along the contour of moisture in the high moisture gradient area and moved eastward with the high-temperature area. The increase in the height and depth of the boundary was mainly supported by the temperature difference between the desert and irrigated areas. In the afternoon, strengthening of the northerly wind due to the approaching shortwave trough converged with the southerly wind and further strengthened the boundary. At the boundary, moisture and heat converged horizontally and were transferred toward the top of the PBL, which represented a critical factor for the development of deep moist convection initiation in the afternoon.

Convection initiation associated with the boundary was suitably captured in the convection-permitting simulation. One

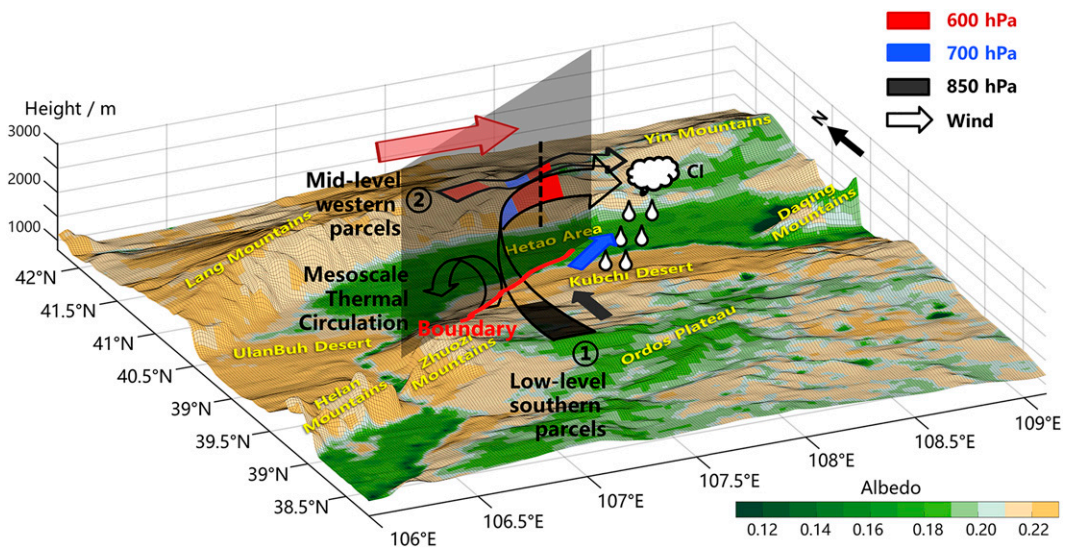

FIG. 19. Summary schematic diagram of the mechanism of CI associated with the boundary, including albedo (shading), topography (surface height), boundary (red line), winds at 600 hPa (red arrow), 700 hPa (blue arrow), 850 hPa (black arrow), and sources of parcels from the CI region and mesoscale thermal circulation (empty arrows). The gray transparent surface indicates the vertical surface along the boundary. The region names are shown in yellow.

unique and interesting finding of this work is that the first 30-dBZ parcels in the different cells exhibited different sources even though these parcels were all lifted by the boundary to some extent, revealing different and more complicated features than those determined in previous studies mainly using idealized frameworks. These results demonstrated that the sources of the first 30-dBZ air parcels were affected by both boundary lifting and direction changes in environmental flow. In the desert area to the southeast of the boundary, the low-level southerly wind turned into a middle-level southwesterly wind and high-level westerly wind, while in the area to the northwest of the boundary, the low-level northwesterly wind turned into a middle-level southwesterly wind and high-level westerly wind. As a result, parcels originating from the west were affected by the boundary for a shorter time and could be lifted only across a smaller vertical distance, especially for the parcels from the low-level west, while the southern low-level parcels veered above the boundary, experiencing a longer uplift time by the boundary. Therefore, only the middle-level parcels originating from the west and low-level parcels stemming from the south reached their LFC first. Trajectories that began in the updraft core were generally consistent with the main conclusions drawn from trajectories starting in the 30-dBZ reflectivities about the boundary effect on CI.

A schematic diagram of CI in association with the boundary was proposed in this case (Fig. 19). The CI process was triggered by the boundary generated through the convergence between background southerly winds and the oasis breeze of the mesoscale thermal circulation produced by the vegetation contrast. The different cells triggered along the boundary exhibited different sources of air parcels. Changes in the background wind direction at the different levels led to parcels originating from different sources being lifted by the boundary for different durations, resulting in middle-level oasis parcels from the west and low-level desert parcels from the south first reaching their LFC, rather than from the low-level oasis breeze, as revealed in previous idealized studies.

Considering that the initiation process involving multiple cells without apparent interaction exhibited notable commonality, the schematic diagram proposed in this study may largely represent the impact of the boundary over the Kubchi Desert on CI in an environment with low-level southerly winds, middle-level southwesterly winds, and high-level westerly winds over the Kubchi Desert area. Further research on the mechanism of CI will be conducted considering different synoptic environments and different background winds. In addition, this case study was limited by the sparse observational data for Hetao and nearby areas. With the launch of a field experiment in the Hetao area from 5 July to 9 August 2022, led by the corresponding author of this work, the formation mechanism of the boundary and its impact on CI in the Hetao area will be examined with more detailed observations.

Acknowledgments. We would like to thank the editor and three anonymous reviewers very much for their insightful suggestions and comments that have greatly improved the quality of this work. This work was sponsored by the National Natural Science Foundation of China (Grants 42030604 and 41905049).

Data availability statement. Radar data and surface observations were provided by the National Meteorological Information Center of the China Meteorological Administration (https://data.cma.cn/data/cdcindex/cid/0b9164954813c573.html). The ERA5 data used in this work (Hersbach et al. 2018a,b for data on pressure and single levels; Muñoz Sabater 2019 for data of land variables) are freely available on the Copernicus

Data Store (CDS) at https://cds.climate.copernicus.eu/cdsapp#!/search?type=dataset. The FNL data (National Centers for Environmental Prediction/National Weather Service/NOAA/U.S. Department of Commerce 2000) are obtained from https://rda.ucar.edu/datasets/ds083.2/. The MODIS data (MOD13A3-V006; Didan 2015) were downloaded from NASA's Earth Observing System Data and Information System (EOSDIS; https://search.earthdata.nasa.gov/search).

REFERENCES

Arritt, R. W., 1993: Effects of the large-scale flow on characteristic features of the sea breeze. *J. Appl. Meteor.*, **32**, 116–125, https://doi.org/10.1175/1520-0450(1993)032<0116:EOTLSF>2.0.CO;2.

Atkins, N. T., and R. M. Wakimoto, 1997: Influence of the synoptic-scale flow on sea breezes observed during CaPE. *Mon. Wea. Rev.*, **125**, 2112–2130, https://doi.org/10.1175/1520-0493(1997)125<2112:IOTSSF>2.0.CO;2.

Baker, R. D., B. H. Lynn, A. Boone, W.-K. Tao, and J. Simpson, 2001: The influence of soil moisture, coastline curvature, and land-breeze circulations on sea-breeze-initiated precipitation. *J. Hydrometeor.*, **2**, 193–211, https://doi.org/10.1175/1525-7541(2001)002<0193:TIOSMC>2.0.CO;2.

Bennett, L. J., K. A. Browning, A. M. Blyth, D. J. Parker, and P. A. Clark, 2006: A review of the initiation of precipitating convection in the United Kingdom. *Quart. J. Roy. Meteor. Soc.*, **132**, 1001–1020, https://doi.org/10.1256/qj.05.54.

Betts, R. A., 2000: Offset of the potential carbon sink from boreal forestation by decreases in surface albedo. *Nature*, **408**, 187–190, https://doi.org/10.1038/35041545.

Birch, C. E., D. J. Parker, A. O'Leary, J. H. Marsham, C. M. Taylor, P. P. Harris, and G. M. S. Lister, 2013: Impact of soil moisture and convectively generated waves on the initiation of a West African mesoscale convective system. *Quart. J. Roy. Meteor. Soc.*, **139**, 1712–1730, https://doi.org/10.1002/qj.2062.

Chen, X., F. Zhang, and K. Zhao, 2016: Diurnal variations of the land–sea breeze and its related precipitation over South China. *J. Atmos. Sci.*, **73**, 4793–4815, https://doi.org/10.1175/JAS-D-16-0106.1.

Collins, W. D., and Coauthors, 2004: Description of the NCAR Community Atmosphere Model (CAM 3.0). NCAR Tech. Note NCAR/TN-464+STR, 214 pp., https://doi.org/10.5065/D63N21CH.

Comer, N. T., and I. G. Mckendry, 1993: Observations and numerical modelling of Lake Ontario breezes. *Atmos.–Ocean*, **31**, 481–499, https://doi.org/10.1080/07055900.1993.9649482.

Courault, D., P. Drobinski, Y. Brunet, P. Lacarrere, and C. Talbot, 2007: Impact of surface heterogeneity on a buoyancy-driven convective boundary layer in light winds. *Bound.-Layer Meteor.*, **124**, 383–403, https://doi.org/10.1007/s10546-007-9172-y.

Crosman, E. T., and J. D. Horel, 2010: Sea and lake breezes: A review of numerical studies. *Bound.-Layer Meteor.*, **137**, 1–29, https://doi.org/10.1007/s10546-010-9517-9.

Davies-Jones, R., R. J. Trapp, and H. B. Bluestein, 2001: Tornadoes and tornadic storms. *Severe Convective Storms*, C. A. Doswell III, Ed., Amer. Meteor. Soc., 167–221.

Didan, K., 2015: MOD13A3 MODIS/Terra vegetation Indices Monthly L3 Global 1km SIN Grid V006. NASA EOSDIS Land Processes DAAC, accessed 10 October 2019, https://doi.org/10.5067/MODIS/MOD13A3.006.

Doswell, C. A., III, 2005: A primer on vorticity for application in supercells and tornadoes. Cooperative Institute for Mesoscale Meteorological Studies, accessed 1 February 2022, http://www.flame.org/~cdoswell/vorticity/vorticity_primer.html.

Dou, J., Y. Wang, R. Bornstein, and S. Miao, 2015: Observed spatial characteristics of Beijing urban climate impacts on summer thunderstorms. *J. Appl. Meteor. Climatol.*, **54**, 94–105, https://doi.org/10.1175/JAMC-D-13-0355.1.

Doviak, R. J., and D. S. Zrnić, 1993: *Doppler Radar and Weather Observations*. 2nd ed. Academic Press, 562 pp.

Estoque, M. A., 1981: Further studies of a lake breeze Part I: Observational study. *Mon. Wea. Rev.*, **109**, 611–618, https://doi.org/10.1175/1520-0493(1981)109<0611:FSOALB>2.0.CO;2.

Fovell, R. G., 2005: Convective initiation ahead of the sea-breeze front. *Mon. Wea. Rev.*, **133**, 264–278, https://doi.org/10.1175/MWR-2852.1.

Franchito, S. H., V. B. Rao, J. L. Stech, and J. A. Lorenzzetti, 1998: The effect of coastal upwelling on the sea-breeze circulation at Cabo Frio, Brazil: A numerical experiment. *Ann. Geophys.*, **16**, 866–871, https://doi.org/10.1007/s00585-998-0866-3.

Gambill, L. D., and J. R. Mecikalski, 2011: A satellite-based summer convective cloud frequency analysis over the southeastern United States. *J. Appl. Meteor. Climatol.*, **50**, 1756–1769, https://doi.org/10.1175/2010JAMC2559.1.

Garcia-Carreras, L., D. J. Parker, C. M. Taylor, C. E. Reeves, and J. G. Murphy, 2010: Impact of mesoscale vegetation heterogeneities on the dynamical and thermodynamic properties of the planetary boundary layer. *J. Geophys. Res.*, **115**, D03102, https://doi.org/10.1029/2009JD012811.

——, ——, and J. H. Marsham, 2011: What is the mechanism for the modification of convective cloud distributions by land surface–induced flows? *J. Atmos. Sci.*, **68**, 619–634, https://doi.org/10.1175/2010JAS3604.1.

Gille, S. T., 2005: Global observations of the land breeze. *Geophys. Res. Lett.*, **32**, L05605, https://doi.org/10.1029/2004GL022139.

Goldreich, Y., L. M. Druyan, and H. Berger, 1986: The interaction of valley/mountain winds with a diurnally veering sea/land breeze. *J. Climatol.*, **6**, 551–561, https://doi.org/10.1002/joc.3370060508.

Grell, G. A., and S. R. Freitas, 2014: A scale and aerosol aware stochastic convective parameterization for weather and air quality modeling. *Atmos. Chem. Phys.*, **14**, 5233–5250, https://doi.org/10.5194/acp-14-5233-2014.

Hersbach, H., and Coauthors, 2018a: ERA5 hourly data on pressure levels from 1959 to present. Copernicus Climate Change Service (C3S) Climate Data Store (CDS), accessed 10 October 2019, https://doi.org/10.24381/cds.bd0915c6.

——, and Coauthors, 2018b: ERA5 hourly data on single levels from 1959 to present. Copernicus Climate Change Service (C3S) Climate Data Store (CDS), accessed 10 October 2019, https://doi.org/10.24381/cds.adbb2d47.

Huang, W.-R., J. C. L. Chan, and S.-Y. Wang, 2010: A planetary-scale land-sea breeze circulation in East Asia and the western North Pacific. *Quart. J. Roy. Meteor. Soc.*, **136**, 1543–1553, https://doi.org/10.1002/qj.663.

Huang, Y., Z. Meng, W. Li, L. Bai, and X. Meng, 2019: General features of radar-observed boundary layer convergence lines and their associated convection over a sharp vegetation-contrast area. *Geophys. Res. Lett.*, **46**, 2865–2873, https://doi.org/10.1029/2018GL081714.

——, ——, and M. Zhang, 2022: Synoptic impacts on the occurrence of mesoscale boundaries and their associated convection over an area of sharp vegetation contrast. *Geophys. Res. Lett.*, **49**, e2022GL099449, https://doi.org/10.1029/2022GL099449.

Kang, S.-L., and G. H. Bryan, 2011: A large-eddy simulation study of moist convection initiation over heterogeneous surface fluxes. *Mon. Wea. Rev.*, **139**, 2901–2917, https://doi.org/10.1175/MWR-D-10-05037.1.

——, and J.-H. Ryu, 2016: Response of moist convection to multi-scale surface flux heterogeneity. *Quart. J. Roy. Meteor. Soc.*, **142**, 2180–2193, https://doi.org/10.1002/qj.2811.

Kawase, H., T. Yoshikane, M. Hara, F. Kimura, T. Sato, and S. Ohsawa, 2008: Impact of extensive irrigation on the formation of cumulus clouds. *Geophys. Res. Lett.*, **35**, L01806, https://doi.org/10.1029/2007GL032435.

Keen, C. S., and W. A. Lyons, 1978: Lake/land breeze circulations on the western shore of Lake Michigan. *J. Appl. Meteor.*, **17**, 1843–1855, https://doi.org/10.1175/1520-0450(1978)017<1843:LBCOTW>2.0.CO;2.

Koch, S. E., and C. A. Ray, 1997: Mesoanalysis of summertime convergence zones in central and eastern North Carolina. *Wea. Forecasting*, **12**, 56–77, https://doi.org/10.1175/1520-0434(1997)012<0056:MOSCZI>2.0.CO;2.

Koseki, S., and P. A. Mooney, 2019: Influences of Lake Malawi on the spatial and diurnal variability of local precipitation. *Hydrol. Earth Syst. Sci.*, **23**, 2795–2812, https://doi.org/10.5194/hess-23-2795-2019.

Laird, N. F., D. A. R. Kristovich, X.-Z. Liang, R. W. Arritt, and K. Labas, 2001: Lake Michigan lake breezes: Climatology, local forcing, and synoptic environment. *J. Appl. Meteor.*, **40**, 409–424, https://doi.org/10.1175/1520-0450(2001)040<0409:LMLBCL>2.0.CO;2.

Lee, J. M., Y. Zhang, and S. A. Klein, 2019: The effect of land surface heterogeneity and background wind on shallow cumulus clouds and the transition to deeper convection. *J. Atmos. Sci.*, **76**, 401–419, https://doi.org/10.1175/JAS-D-18-0196.1.

Liang, Z., D. Wang, Y. Liu, and Q. Cai, 2017: A numerical study of the convection triggering and propagation associated with sea breeze circulation over Hainan Island. *J. Geophys. Res. Atmos.*, **122**, 8567–8592, https://doi.org/10.1002/2016JD025915.

Lin, C.-Y., F. Chen, J. C. Huang, W.-C. Chen, Y.-A. Liou, W.-N. Chen, and S.-C. Liu, 2008: Urban heat island effect and its impact on boundary layer development and land–sea circulation over northern Taiwan. *Atmos. Environ.*, **42**, 5635–5649, https://doi.org/10.1016/j.atmosenv.2008.03.015.

Lu, H., Y. Liu, A. Liu, N. Zhang, and M. Sun, 2012: Study of thunderstorm initiation and intensification rules associated with sea breeze fronts. *Meteor. Mon.*, **38**, 1078–1086.

Lu, R., and R. P. Turco, 1994: Air pollutant transport in a coastal environment. Part I: Two-dimensional simulations of sea-breeze and mountain effects. *J. Atmos. Sci.*, **51**, 2285–2308, https://doi.org/10.1175/1520-0469(1994)051<2285:APTIAC>2.0.CO;2.

Lu, X., K.-C. Chow, T. Yao, A. K. H. Lau, and J. C. H. Fung, 2010: Effects of urbanization on the land sea breeze circulation over the Pearl River Delta region in winter. *Int. J. Climatol.*, **30**, 1089–1104, https://doi.org/10.1002/joc.1947.

Lyons, T. J., R. C. G. Smith, and H. Xinmei, 1996: The impact of clearing for agriculture on the surface energy budget. *Int. J. Climatol.*, **16**, 551–558, https://doi.org/10.1002/(SICI)1097-0088(199605)16:5<551::AID-JOC25>3.0.CO;2-9.

Marion, G. R., and R. J. Trapp, 2019: The dynamical coupling of convective updrafts, downdrafts, and cold pools in simulated supercell thunderstorms. *J. Geophys. Res. Atmos.*, **124**, 664–683, https://doi.org/10.1029/2018JD029055.

Markowski, P., and Y. Richardson, 2011: *Mesoscale Meteorology in Midlatitudes*. Vol. 2. Wiley-Blackwell, 407 pp.

Meng, X., Y. Sun, R. Sa, H. Yuan, and S. Ha, 2013: Correlation between eastward developing of Hetao cyclone and the severe rainstorm in Beijing on 21 July 2012. *Meteor. Mon.*, **39**, 1542–1549.

Miller, S. T. K., B. D. Keim, R. W. Talbot, and H. Mao, 2003: Sea breeze: Structure, forecasting, and impacts. *Rev. Geophys.*, **41**, 1011, https://doi.org/10.1029/2003RG000124.

Morrison, H., G. Thompson, and V. Tatarskii, 2009: Impact of cloud microphysics on the development of trailing stratiform precipitation in a simulated squall line: Comparison of one- and two-moment schemes. *Mon. Wea. Rev.*, **137**, 991–1007, https://doi.org/10.1175/2008MWR2556.1.

Muñoz Sabater, J., 2019: ERA5-Land hourly data from 1950 to present. Copernicus Climate Change Service (C3S) Climate Data Store (CDS), accessed 10 October 2019, https://doi.org/10.24381/cds.e2161bac.

National Centers for Environmental Prediction/National Weather Service/NOAA/U.S. Department of Commerce, 2000: NCEP FNL Operational Model Global Tropospheric Analyses, continuing from July 1999. Research Data Archive at the National Center for Atmospheric Research, Computational and Information Systems Laboratory, accessed 10 October 2019, https://doi.org/10.5065/D6M043C6.

National Geophysical Data Center/NESDIS/NOAA/U.S. Department of Commerce, 2011: ETOPO1, Global 1 Arc-minute Ocean Depth and Land Elevation from the US National Geophysical Data Center (NGDC). Research Data Archive at the National Center for Atmospheric Research, Computational and Information Systems Laboratory, accessed 10 October 2019, https://doi.org/10.5065/D69Z92Z5.

Ookouchi, Y., M. Segal, R. C. Kessler, and R. A. Pielke, 1984: Evaluation of soil moisture effects on the generation and modification of mesoscale circulations. *Mon. Wea. Rev.*, **112**, 2281–2292, https://doi.org/10.1175/1520-0493(1984)112<2281:EOSMEO>2.0.CO;2.

Pielke, R. A., 2001: Influence of the spatial distribution of vegetation and soils on the prediction of cumulus convective rainfall. *Rev. Geophys.*, **39**, 151–177, https://doi.org/10.1029/1999RG000072.

Pleim, J. E., 2006: A simple, efficient solution of flux–profile relationships in the atmospheric surface layer. *J. Appl. Meteor. Climatol.*, **45**, 341–347, https://doi.org/10.1175/JAM2339.1.

——, 2007: A combined local and nonlocal closure model for the atmospheric boundary layer. Part II: Application and evaluation in a mesoscale meteorological model. *J. Appl. Meteor. Climatol.*, **46**, 1396–1409, https://doi.org/10.1175/JAM2534.1.

——, and A. Xiu, 1995: Development and testing of a surface flux and planetary boundary-layer model for application in mesoscale models. *J. Appl. Meteor.*, **34**, 16–32, https://doi.org/10.1175/1520-0450-34.1.16.

Porson, A., D. G. Steyn, and G. Schayes, 2007: Sea-breeze scaling from numerical model simulations, part II: Interaction between the sea breeze and slope flows. *Bound.-Layer Meteor.*, **122**, 31–41, https://doi.org/10.1007/s10546-006-9092-2.

Qian, T., C. C. Epifanio, and F. Zhang, 2012: Topographic effects on the tropical land and sea breeze. *J. Atmos. Sci.*, **69**, 130–149, https://doi.org/10.1175/JAS-D-11-011.1.

Qu, X., Q. Yang, H. Wang, Q. Cao, and C. Lin, 2019: Characteristics of meteorological drought intensity in inner Mongolia based on MCI. *Meteor. Environ. Sci.*, **42**, 47–54.

Rani, S. I., R. Ramachandran, D. B. Subrahamanyam, D. P. Alappattu, and P. K. Kunhikrishnan, 2010: Characterization of sea/land breeze circulation along the west coast of Indian

sub-continent during pre-monsoon season. *Atmos. Res.*, **95**, 367–378, https://doi.org/10.1016/j.atmosres.2009.10.009.

Rotunno, R., and J. B. Klemp, 1982: The influence of the shear-induced pressure gradient on thunderstorm motion. *Mon. Wea. Rev.*, **110**, 136–151, https://doi.org/10.1175/1520-0493(1982)110<0136:TIOTSI>2.0.CO;2.

Sato, T., F. Kimura, and A. S. Hasegawa, 2007: Vegetation and topographic control of cloud activity over arid/semiarid Asia. *J. Geophys. Res.*, **112**, D24109, https://doi.org/10.1029/2006JD008129.

Seth, A., and F. Giorgi, 1996: Three-dimensional model study of organized mesoscale circulations induced by vegetation. *J. Geophys. Res.*, **101**, 7371–7391, https://doi.org/10.1029/95JD02677

Skamarock, W. C., and Coauthors, 2008: A description of the Advanced Research WRF version 3. NCAR Tech. Note NCAR/TN-475+STR, 113 pp., https://doi.org/10.5065/D68S4MVH.

Taylor, C. M., D. J. Parker, and P. P. Harris, 2007: An observational case study of mesoscale atmospheric circulations induced by soil moisture. *Geophys. Res. Lett.*, **34**, L15801, https://doi.org/10.1029/2007GL030572.

——, P. P. Harris, and D. J. Parker, 2010: Impact of soil moisture on the development of a Sahelian mesoscale convective system: A case-study from the AMMA Special Observing Period. *Quart. J. Roy. Meteor. Soc.*, **136** (Suppl. 1), 456–470, https://doi.org/10.1002/qj.465.

——, A. Gounou, F. Guichard, P. P. Harris, R. J. Ellis, F. Couvreux, and M. De Kauwe, 2011: Frequency of Sahelian storm initiation enhanced over mesoscale soil-moisture patterns. *Nat. Geosci.*, **4**, 430–433, https://doi.org/10.1038/ngeo1173.

Tian, L., Y. Zhang, and J. Zhu, 2014: Decreased surface albedo driven by denser vegetation on the Tibetan Plateau. *Environ. Res. Lett.*, **9**, 104001, https://doi.org/10.1088/1748-9326/9/10/104001.

Tian, Y., and J. Miao, 2019: A numerical study of mountain-plain breeze circulation in eastern Chengdu, China. *Sustainability*, **11**, 2821, https://doi.org/10.3390/su11102821.

Wang, C., W. Tian, D. J. Parker, J. H. Marsham, and Z. Guo, 2011: Properties of a simulated convective boundary layer over inhomogeneous vegetation. *Quart. J. Roy. Meteor. Soc.*, **137**, 99–117, https://doi.org/10.1002/qj.724.

Wang, D., J. Miao, and D.-L. Zhang, 2015: Numerical simulations of local circulation and its response to land cover changes over the Yellow Mountains of China. *J. Meteor. Res.*, **29**, 667–681, https://doi.org/10.1007/s13351-015-4070-6.

Weckwerth, T. M., and D. B. Parsons, 2006: A review of convection initiation and motivation for IHOP_2002. *Mon. Wea. Rev.*, **134**, 5–22, https://doi.org/10.1175/MWR3067.1.

Wilson, J. W., and W. E. Schreiber, 1986: Initiation of convective storms at radar-observed boundary-layer convergence lines. *Mon. Wea. Rev.*, **114**, 2516–2536, https://doi.org/10.1175/1520-0493(1986)114<2516:IOCSAR>2.0.CO;2.

——, and R. D. Roberts, 2006: Summary of convective storm initiation and evolution during IHOP: Observational and modeling perspective. *Mon. Wea. Rev.*, **134**, 23–47, https://doi.org/10.1175/MWR3069.1.

Wright, J. S., R. Fu, J. R. Worden, S. Chakraborty, N. E. Clinton, C. Risi, Y. Sun, and L. Yin, 2017: Rainforest-initiated wet season onset over the southern Amazon. *Proc. Natl. Acad. Sci. USA*, **114**, 8481–8486, https://doi.org/10.1073/pnas.1621516114.

Xiu, A. J., and J. E. Pleim, 2001: Development of a land surface model. Part I: Application in a mesoscale meteorological model. *J. Appl. Meteor.*, **40**, 192–209, https://doi.org/10.1175/1520-0450(2001)040<0192:DOALSM>2.0.CO;2.

Yu, B., B. Zhu, S. Miao, H. Kang, X. He, H. Liu, Z. Liang, and F. Chen, 2021: Observational signal of the interaction between mountain–plain wind and urban breeze under weak synoptic systems. *J. Geophys. Res. Atmos.*, **126**, e2020JD032809, https://doi.org/10.1029/2020JD032809.

Yu, H., and Z. Meng, 2016: Key synoptic-scale features influencing the high-impact heavy rainfall in Beijing, China, on 21 July 2012. *Tellus*, **68A**, 31045, https://doi.org/10.3402/tellusa.v68.31045.

Yu, X., 2012: Investigation of Beijing extreme flooding event on 21 July 2012. *Meteor. Mon.*, **38**, 1313–1329.

Zamuriano, M., A. Martynov, L. Panziera, and S. Brönnimann, 2019: Characteristics of a hailstorm over the Andean La Paz Valley. *Nat. Hazards Earth Syst. Sci. Discuss.*, [preprint], https://doi.org/10.5194/nhess-2019-27.

Zhang, D., J. Zhan, Z. Qiao, and R. Župan, 2020: Evaluation of the performance of the integration of remote sensing and Noah hydrologic model for soil moisture estimation in Hetao irrigation region of inner Mongolia. *Can. J. Remote Sens.*, **46**, 552–566, https://doi.org/10.1080/07038992.2020.1810003.

Zhang, Y., and S. A. Klein, 2010: Mechanisms affecting the transition from shallow to deep convection over land: Inferences from observations of the diurnal cycle collected at the ARM southern Great Plains Site. *J. Atmos. Sci.*, **67**, 2943–2959, https://doi.org/10.1175/2010JAS3366.1.